Title: Type-I nNOS neurons orchestrate cortical neural activity and vasomotion

Authors: Kevin L. Turner[1,2,3.7], Dakota F. Brockway[4,7], Md Shakhawat Hossain[2,3,7], Keith R. Griffith[4,7], Denver I. Greenawalt[5,7], Qingguang Zhang[1,2,7,8], Kyle W. Gheres[1,2,7], Nicole A. Crowley[2,3,4,7], Patrick J. Drew[1,2,3,6,7]

Affiliations:

1. Department of Engineering Science and Mechanics, The Pennsylvania State University, University Park, PA 16802
2. Center for Neural Engineering, The Pennsylvania State University, University Park, PA 16802
3. Department of Biomedical Engineering, The Pennsylvania State University, University Park, PA 16802
4. Department of Biology, The Pennsylvania State University, University Park, PA 16802
5. Graduate Program in Molecular Cellular and Integrative Biosciences, The Pennsylvania State University, University Park, PA 16802
6. Department of Neurosurgery, The Pennsylvania State University, University Park, PA 16802
7. Penn State Neuroscience Institute, The Pennsylvania State University, University Park, PA 16802
8. Department of Physiology, Michigan State University, East Lansing, MI 48824

***Corresponding author:** Patrick J. Drew - pjd17@psu.edu

Acknowledgements: This work was supported by NIH Grants R01NS078168, R01NS079737, U19NS128613 to PJD, R01AA029403 to NAC, an American Heart Association Predoctoral fellowship 24PRE1201066 to MSH and F31ES036154 to DIG. DIG was supported by T32GM108563 and MSH was supported by T32NS115667.

Conflict of Interest: The authors declare no competing financial interests.

Author Contributions K.L.T, N.A.C, and P.J.D. designed the experiments. K.L.T, D.F.B, M.S.H, K.R.G, D.I.G, and Q.Z performed experiments. K.L.T., M.S.H, Q.Z, K.W.G., and P.J.D. analyzed the data. K.L.T. and P.J.D. wrote the paper.

Abstract: It is unknown how the brain orchestrates coordination of global neural and vascular dynamics. We sought to uncover the role of a sparse but unusual population of genetically-distinct interneurons known as type-I nNOS neurons, using a novel pharmacological strategic to unilaterally ablate these neurons from the somatosensory cortex of mice. Region-specific ablation produced changes in both neural activity and vascular dynamics, decreased power in the delta-band of the local field potential, reduced sustained vascular responses to prolonged sensory stimulation, and abolished the post-stimulus undershoot in cerebral blood volume. Coherence between the left and right somatosensory cortex gamma-band power envelope and blood volume at ultra-low frequencies was decreased, suggesting type-1 nNOS neurons integrate long-range coordination of brain signals. Lastly, we observed decreases in the amplitude of resting-state blood volume oscillations and decreased vasomotion following the ablation of type-I nNOS neurons. This demonstrates that a small population of nNOS-positive neurons are indispensable for regulating both neural and vascular dynamics in the whole brain and implicates disruption of these neurons in diseases ranging from neurodegeneration to sleep disturbances.

Keywords: neurovascular coupling, type-I nNOS neurons, somatosensory cortex, two-photon, cerebral blood volume, widefield optical imaging, sleep

Introduction

Coordinated neural and hemodynamic activity across the brain are vital for arousal and cognition. The relationship between changes in neural activity and (typically measured) changes in blood volume, flow, and oxygenation, which are frequently studied with hemodynamic imaging and form the foundation of modern neuroscience, are mediated by local vasodilation and is known as neurovascular coupling (Drew, 2019a; Schaeffer, 2021). The vasodilator nitric oxide (NO) (Hosford, 2019), produced by neuronal nitric oxide synthase (nNOS) in neurons, provides a key mechanism of arteriole dilation. Neurons in somatosensory cortex that express nNOS are activated by sensory stimulation, volitional whisking, and locomotion (Echagarruga, 2020; Ahn, 2023), all of which produce robust hemodynamic responses (Huo, 2014; Winder, 2017). Chemogenetic elevation or suppression of nNOS neuron activity alters both baseline diameter and behaviorally-evoked dilation of arterioles (Echagarruga, 2020). Similar vascular changes are produced by local infusion of a NOS inhibitor (Echagarruga, 2020), implicating NO signaling directly in vascular regulation. Optogenetic activation of nNOS-positive neurons produces varying effects, with some reports demonstrating vasodilation and blood flow increases with minimal changes in neural activity (Krawchuk, 2020; Lee, 2020; Ruff, 2024), while others show large, low-frequency EEG changes during sleep and quiet wakeful states (Gerashchenko, 2018). While NO is known to modulate the excitability of neurons (Kara, 1999; Smith, 2003), artificial activation of nNOS neurons seems to drive vascular responses that are disproportionally larger than any corresponding neural changes, suggesting that this small population of neurons has an impact on vascular signals that is substantially greater than that of overall neural activity.

Two distinct GABAergic interneurons types express nNOS, denoted as type-I and type-II (Kawaguchi, 1997; Kubota, 2011; Perrenoud, 2012). nNOS-positive neurons make up approximately 20% of GABAergic interneurons in the cortex (Hendry, 1987; Sahara, 2012), with type-I constituting only 0.5–2% depending on brain region (Yan, 1997; Tricoire, 2012; Chong, 2019). Type-I nNOS neurons are sparse, somatostatin-positive, most dense in the deep layers of cortex, and express nNOS at higher levels than type-II. They extend both local and long-range projections throughout the cortex, receive excitatory input from nearby pyramidal neurons and drive increases in cerebral blood flow when stimulated (Ruff, 2024). Type-II nNOS neurons are in contrast much more abundant, smaller in size and morphology, and express nNOS less strongly than type-I. Type-II are a more heterogeneous group that express a variety of interneuron subtype markers and are more evenly distributed throughout the different layers of cortex (Yan, 1996; Perrenoud, 2012). Type-I nNOS neurons have been observed in rodents, carnivores, and primates (Tomioka, 2005; Higo, 2007; Tomioka, 2007) and are active during sleep (Gerashchenko, 2008; Kilduff, 2011; Morairty, 2013; Dittrich, 2015). In the cortex, type-I nNOS neuron density is anticorrelated with vascular density (Wu, 2022). Type-I nNOS neurons integrate local activity from feedforward excitatory pathways from the cortex and thalamus, likely contributing to the correlated changes in blood flow that are observed between functionally connected regions across hemispheres (Ruff, 2024). Molecular, electrophysiological, and immunohistochemistry studies have demonstrated that type-I nNOS neurons are the only cells in the cortex that express the tachykinin receptor 1 (also known as neurokinin 1 receptor, TACR1/NK1R), the primary receptor for the endogenous

neuropeptide substance P (Penny, 1986; Vruwink, 2001; Kubota, 2011; Dittrich, 2012; Endo, 2016; He, 2016; Huang, 2016; Paul, 2017; Vanlandewijck, 2018; Matsumura, 2021; Ruff, 2024). Local infusion of substance P into the cortex causes a sustained increase in basal arterial diameter that is dependent upon local neural activity (Echagarruga, 2020). Type-I nNOS neurons likely receive substance P from the ~40% of parvalbumin (PV)-positive cortical interneurons (Vruwink, 2001; Pfeffer, 2013; Bugeon, 2022) that are thought to drive network synchrony (Cardin, 2009; Sohal, 2009). Optogenetic stimulation of PV neurons for several seconds drives a biphasic hemodynamic response, comprised of an early constriction (driven by suppression of overall population activity through GABA release), and a delayed, prolonged dilation lasting tens of seconds that is mediated indirectly by substance P (Vo, 2023). The delayed vasodilation was not directly related to pyramidal neuron activity, was blocked by TACR1 antagonists, and was occluded by substance P, suggesting that activation of PV neurons drives downstream activation of type-I nNOS neurons. These experiments point to type-I nNOS neurons as having a large effect on vascular dynamics despite their smaller contribution in driving overall neural activity. However, optogenetic stimulation only activates one component of a circuit in isolation, in an otherwise healthy and intact microcircuit, potentially giving an incomplete picture of the neuron's role. Type-I nNOS neurons are uniquely vulnerable to stress (Han, 2019), and their loss is likely in part causal to neurodegeneration (Schaeffer, 2021; Iadecola, 2023), making it vital to understand brain wide changes following a more physiologically-relevant model of perturbation.

Here we sought to reveal the role of type-I nNOS neurons in controlling neural and vascular dynamics in the cortex by selectively ablating them with saporin conjugated to a substance P analog (SP-saporin). Using this targeted ablation approach, we found that ablation of type-I nNOS neurons caused decreases in the hemodynamic response to sustained vibrissae stimulation, eliminated the post-stimulus undershoot, decreased local field potential power in the delta-band (1-4 Hz), reduced bilateral correlations in gamma-band power and blood volume across arousal states, and reduced the amplitude of resting-state blood volume oscillations. Together, these experiments demonstrate that a small subset of type-I nNOS neurons regulate key neural and vascular dynamics that coordinate changes in vasomotion.

Results

We investigated the effects of localized ablation of type-I nNOS neurons in somatosensory cortex on neurovascular coupling and functional connectivity in unanesthetized, head-fixed mice. C57BL6J mice (119 total, both male and female) were injected with either saporin conjugated to a substance P analog with high affinity for the substance P receptor (SP-SAP) or a scrambled peptide as a control (Blank-SAP) into a localized region of one hemisphere's somatosensory cortex. We used widefield optical imaging, electrophysiology, and 2-photon microscopy to evaluate neural and hemodynamic changes following targeted ablation of type-I nNOS neurons in the vibrissae (whisker) representation of somatosensory cortex while carefully monitoring arousal state (see **Materials and Methods**). All imaging was performed during the animals' light cycle. Statistics included generalized linear

mixed-effects model (GLME), general linear models (GLM), or unpaired t-tests with corrections for multiple comparisons when necessary.

Saporin-conjugated peptides produce selective targeted ablation of type-I nNOS neurons

While optogenetic and chemogenetic models give us insights into the potential function of neuron subtypes, it is difficult to completely silence neurons in vivo, and the patterns of activity they induce are not physiological and can have paradoxical effects on neural activity (Li, 2019; Andrei, 2021). Saporin provides a pharmacological route to

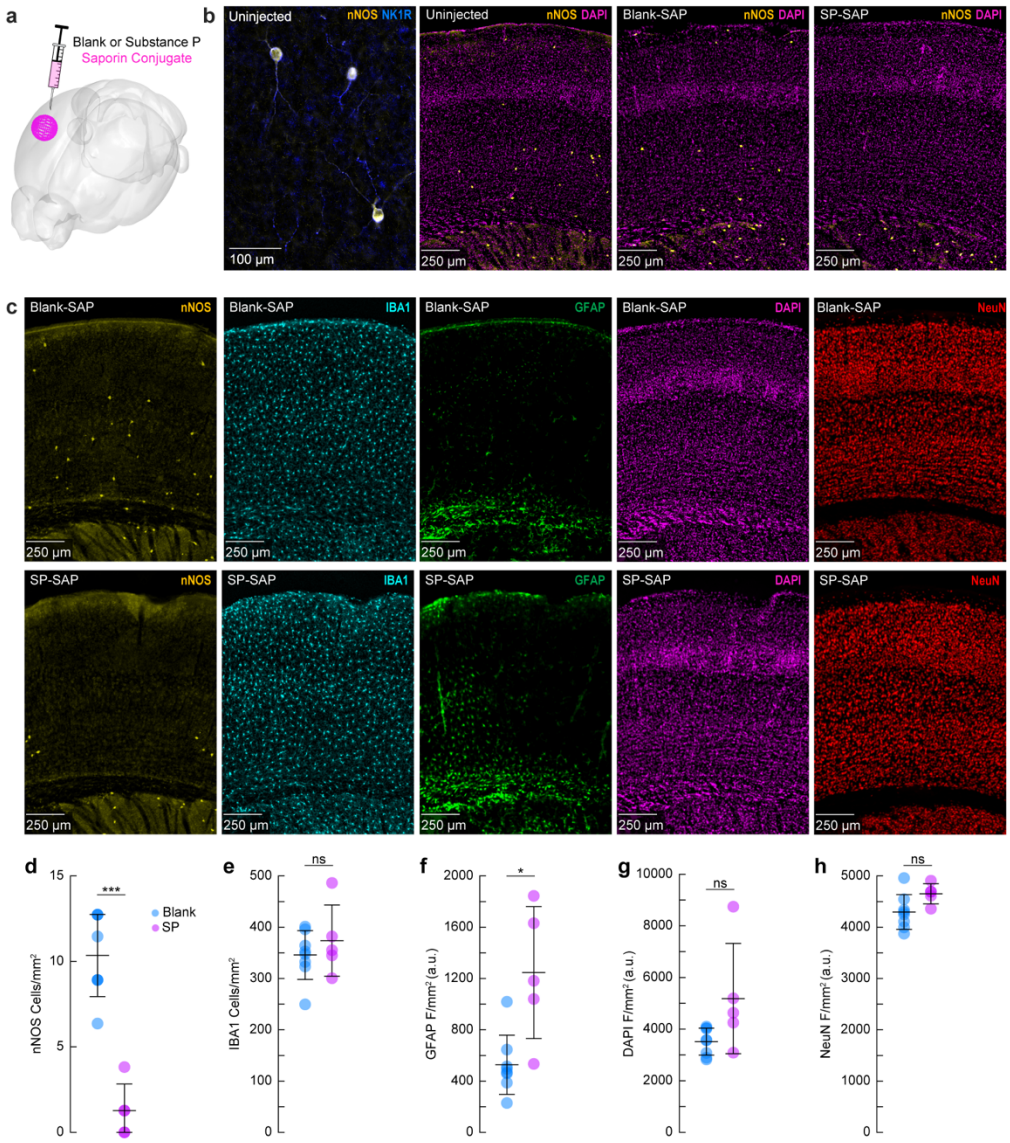

Figure 1. Targeted ablation of type-I nNOS neurons with cortical SP-SAP injections (a) Schematic showing intracortical administration of the ribosome inactivating protein saporin conjugated to either SP or a vehicle control. **(b)** Representative immunofluorescence of anti-nNOS (yellow) and anti-NKR1 (blue) showing colocalization of the NK1 receptor on cortical nNOS-positive neurons. Representative immunofluorescence of anti-nNOS (yellow) and DAPI (magenta) from animals with no injection (Uninjected, left), Blank-SAP (middle), or SP-SAP (right). **(c)** Representative immunofluorescence of Blank-SAP (top) and SP-SAP (bottom) sections co-stained with nNOS (left), IBA1 (middle left), GFAP (middle), DAPI (middle right), or NeuN (right). NeuN image was taken from section immediately adjacent to the first four. **(d)** Quantification of nNOS counts, **(e)** IBA1 counts, **(f)** GFAP fluorescence, **(g)** DAPI fluorescence, **(h)** NeuN fluorescence. Error bars **(d-h)** denote SD. Bonferroni correction (5) *$\alpha < 0.01$, **$\alpha < 0.002$, ***$\alpha < 0.002$. **k-l** *$\alpha < 0.05$, **$\alpha < 0.01$, ***$\alpha < 0.001$, GLME.

111 selectively kill only the cells that internalize it, and saporin conjugated to a peptide effectively targets neurons that
112 express a receptor for the peptide (McKay, 2008; Abbott, 2012), allowing targeting of specific cell types orthogonal
113 to any genetic targeting techniques.

114 We first sought to validate the efficacy and specificity of saporin-based targeting of cortical TACR1-expressing
115 neurons. Type-I nNOS neurons were ablated by injection of the ribosome inactivating protein saporin (SAP),
116 conjugated either to substance P (SP-SAP) or a scrambled peptide as a control (Blank-SAP) (**Fig. 1a**). The SP-bound
117 SAP toxin binds to TACR1-expressing neurons (Wiley, 1999; Martin, 2001; Wang, 2002), which in the cortex are
118 exclusively expressed by type-I nNOS neurons (**Fig. 1b**). We used both immunofluorescence (**Fig. 1c**) and NADPH
119 diaphorase staining (a histochemical marker for NOS, **Fig. S1**), to visualize nNOS neuron ablation (Hope, 1989; Bredt,
120 1991; Hope, 1991). Immunofluorescent labeling in mice injected with Blank-SAP showed labeling of nNOS-positive
121 neurons near the injection site. In contrast, mice injected with SP-SAP showed a clear loss in nNOS-labeling around
122 the injection site, with nNOS-positive neurons both subcortically and in the entirety of the contralateral hemisphere
123 remaining intact. We quantified the efficacy of SP-SAP in removing type-I nNOS neurons by quantifying the number
124 of nNOS-positive neurons per square mm of cortical tissue (**Fig. 1d**), of which SP-SAP injected mice (N = 5, 3M/2F)
125 had a significant reduction of nNOS-labeled neurons (1.3 ± 1.6 neurons/mm^2) compared to Blank-SAP mice (N = 8,
126 4M/4F) with 10.3 ± 2.4 neurons/mm^2 (GLME $p = 5.74\times10^{-6}$).
127 We checked for non-specific effects driven by SP-SAP injections one-month post-administration by staining for
128 ionized calcium binding adaptor molecule 1 (IBA1), glial fibrillary acidic protein (GFAP), DAPI, and NeuN (neuronal
129 nuclei) as well as nNOS (as a positive control for ablation). There was no difference in the number of microglia (**Fig.
130 1e**) between groups (Blank-SAP: 345.8 ± 47.7 microglia/mm^2; SP-SAP: 373.8 ± 69.4 microglia/mm^2). There was an
131 increase in GFAP labeling following SP-SAP injection (1246.3 ± 514.8 AU/mm^2; Blank-SAP: 527.2 ± 230.9 AU/mm^2,
132 GLME $p = 0.0029$) (**Fig. 1f**). There was no significant difference in DAPI fluorescence (Blank-SAP: 3511.2 ± 524.42
133 AU/mm^2; SP-SAP: 5180.7 ± 2135.0 AU/mm^2; GLME $p = 0.038$, **Fig. 1g**) or NeuN fluorescence (Blank-SAP: 4296.8 ±
134 339.4 AU/mm^2; SP-SAP: 4652.1 ± 196.8 AU/mm^2; GLME $p = 0.043$, **Fig. 1h**) between groups after Bonferroni
135 correction for (5) multiple comparisons (**Fig. 1d-h**). Together, these findings indicate that the SP-SAP toxin was highly
136 selective in ablating type-I nNOS neurons with minimal non-specific effects. All mice that underwent imaging were
137 histologically verified for successful type-I nNOS neuron ablation using NADPH diaphorase staining. We quantified a
138 subset of these mice and saw a similar specific removal of type-I nNOS neurons (**Fig. S1)**. To determine if ablation of
139 type-I nNOS neurons from the somatosensory cortex had any impact on behavior or arousal state, we assayed
140 exploratory behavior, sleep, and pupil dynamics (**Fig. S2**). To assay exploratory behavior, mice were placed in a novel
141 open field environment and allowed to explore for 5 minutes while quantifying distance traveled and time spent in
142 the center, two metrics for evaluating stress and anxiety in rodents (Roth, 1979; Seibenhener, 2015). We noted no
143 differences in any metric evaluating open field behavior (N = 12-23 mice/group). We also assessed multiple
144 measurements of sleep quality and quantity. There was no difference in the percentage of time each mouse spent

in rapid eye movement (REM) or non-REM (NREM) sleep, or the percentage of time they spent volitionally whisking while awake (N = 9 mice/group). We also noted no significant differences in eye-related arousal state metrics including interblink-interval, pupil size, and pupillary response to vibrissae stimulation (Turner, 2023). Together, this suggests that ablation of type-I nNOS neurons had no gross effects on sleep or general ambulatory behavior.

Impact of type-I nNOS neuron removal on neural and hemodynamic signals across arousal states

To determine the impact localized ablation of type-I nNOS neurons had on neural and hemodynamic signals in the somatosensory cortex, we used widefield optical imaging (Sirotin, 2009; Huo, 2014) to measure changes in total hemoglobin (Δ[HbT], an indicator of blood volume). We measured neural activity using either implanted electrodes (Winder, 2017) to measure changes in local field potential (LFP) (**Fig. 2a, c, d**), or in a separate cohort of mice, pan-neuronal expression of the calcium indicator GCaMP7s (Chan, 2017; Dana, 2019), which provides complementary measures of bulk neural activity (**Fig. 2b, e, f**). In mice expressing GCaMP7s, we measured Δ[HbT], as well as changes

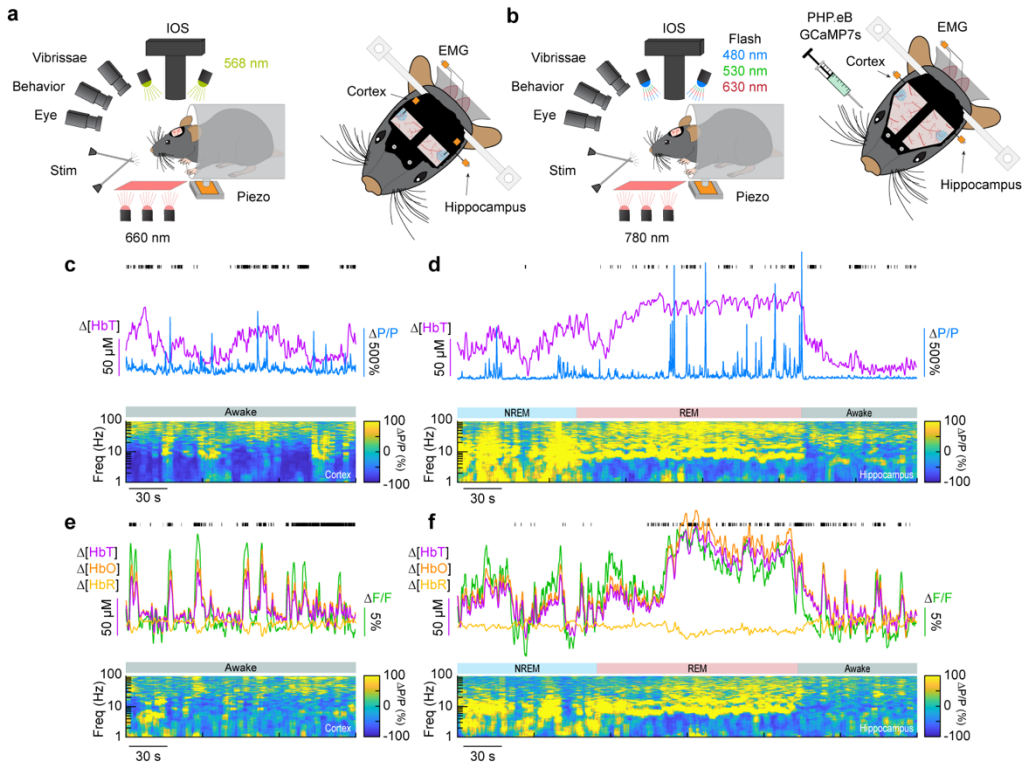

Figure 2. Simultaneous measurement of neural and hemodynamic signals in mice across arousal states (a) Schematic of widefield optical imaging experimental setup. The brain is illuminated at an isosbestic wavelength of hemoglobin (568 nm). Changes in reflected light measuring changes in total blood volume are captured by a camera mounted above the head while several other cameras monitor animal behavior and arousal state including vibrissae and pupil tracking. Vibrissae stimulation is done by directed air puffs. Polished and reinforced thinned-skull windows were bilaterally implanted over the somatosensory cortex. Tungsten stereotrodes were implanted underneath each window to record changes in local field potential within the area of interest. An additional hippocampal stereotrode and a neck electromyography electrode were used to assist in sleep scoring. **(b)** Schematic of widefield optical imaging experiments with GCaMP7s. Alternating illumination with 480 nm, 530 nm, and 630 nm light were used to measure changes in total hemoglobin, blood oxygenation, and GCaMP7s fluorescence. **(c, e)** During the awake state, power in low-frequency cortical LFP is low and power in the gamma-band (30-100 Hz) is elevated during activity such as volitional whisking. **(d, f)** Periods of NREM and REM sleep are accompanied by large oscillations in cerebral blood volume, with large increases in power in delta-band (1-4 Hz) cortical LFP during NREM and large increases in theta-band (4-10 Hz) hippocampal LFP during REM.

in cerebral oxygenation (Δ[HbO]) and deoxygenation (Δ[HbR]) using alternating illumination at 480/530/630 nm (Ma, 2016b; Ma, 2016a; Zhang, 2019). We corrected for hemodynamic contamination of GCaMP7s signals using the simultaneously acquired hemoglobin signals (Kramer, 1979; Ma, 2016b; Wright, 2017; Scott, 2018). Measurements of neural and hemodynamic signals were taken bilaterally through polished and reinforced thinned-skull windows (Drew, 2010; Shih, 2012) in the vibrissae representation of somatosensory cortex. Each animal was habituated to head-fixation over the course of several days following surgery. For the first 60 minutes of each recording session, the vibrissae were briefly stimulated with directed puffs of air to either the left or right pad, or by a puffer directed away from the mouse as an auditory control (Drew, 2011). Afterwards, each mouse was given several hours to naturally sleep with no stimulation. To determine the arousal state of the mouse, we performed electromyography of the nuchal muscles of the neck, tracked vibrissae movement and pupil diameter using video, and body movements with a force sensor. Arousal state was scored in 5 second intervals as either Awake, NREM, or REM as previously described (Turner, 2020) from behavioral and physiological data using a bootstrapped random forest classification algorithm. We saw no differences in the accuracy or validity of our sleep-scoring models across different experimental conditions (Blank-SAP; SP-SAP; Uninjected) (**Fig. S3**).

Ablation of type-I nNOS neurons reduces the stimulus-evoked response

We first determined the impact of removal of type-I nNOS neurons on evoked hemodynamic signals. The initial increase in blood volume in response to brief (0.1 second) stimulation of the contralateral vibrissae was not affected by ablation of type-I nNOS neurons (**Fig. 3a**), but the post-stimulus undershoot was absent in the SP-SAP mice. When we evaluated the canonical post-stimulus hemodynamic undershoot from 2:4 seconds, the Blank-SAP group (N = 9, 5M/4F) had a mean of -2.2 ± 0.5 µM, compared to the SP-SAP group (N = 9, 5M/4F) mean of 1.0 ± 0.6 µM (GLME *p* = 0.0005). This result is consistent with the observation that type-I nNOS neurons express the vasoconstrictory neuropeptide Y (NPY) (Karagiannis, 2009) which is thought to underlie this post-stimulus undershoot (Uhlirova, 2016). It is also possible that loss of NO signaling from type-I nNOS neurons could also contribute through interactions with blood volume to generate oscillations and post-dilation undershoots (Haselden, 2020). Using three-wavelength spectroscopy in mice expressing GCaMP7s, we saw consistent increases in blood volume, neural activity, and cerebral oxygenation during prolonged (5 seconds) vibrissae stimulation. Δ[HbT] evaluated 1.5:6.5 seconds

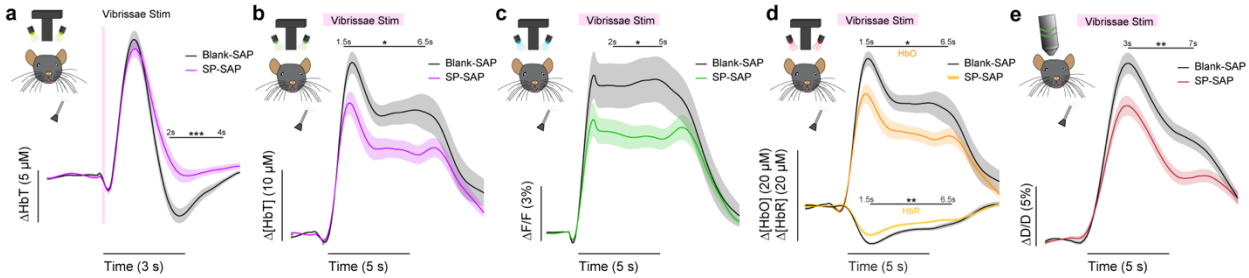

Figure 3. Ablation of type-I nNOS neurons reduces stimulus-evoked hemodynamic responses (a) Change in total hemoglobin in response to brief (0.1 second) vibrissae stimulation. **(b)** Change in total hemoglobin in response to extended (5 seconds) vibrissae stimulation. **(c)** Change in GCaMP fluorescence in response to extended vibrissae stimulation. **(d)** Change in oxy- and deoxy- hemoglobin in response to extended vibrissae stimulation. **(e)** Change in arteriole diameter in response to extended vibrissae stimulation. Error bars represent population averages ± SEM. All statistics were evaluated between the indicated intervals. *p < 0.05, **p < 0.01, ***p < 0.001, GLME.

following stimulus-onset decreased from 18.7 ± 1.7 µM in Blank-SAP (N = 7, 3M/4F) to 13.1 ± 1.4 µM in SP-SAP (N = 8, 4M/4F, GLME p = 0.017) (**Fig. 3b**). Calcium signals (**Fig. 3c**) evaluated 2:5 seconds following stimulus onset decreased from 8.2 ± 1.3 % in Blank-SAP to 5.3 ± 0.7 % in SP-SAP (GLME p = 0.047). Δ[HbO] (**Fig. 3d**) evaluated 1.5:6.5 seconds following stimulus onset decreased from 24.6 ± 1.9 µM in Blank-SAP to 17.4 ± 1.7 µM in SP-SAP (GLME p = 0.010) while Δ[HbR] evaluated from 1.5:6.5 seconds increased from -6.0 ± 0.4 in Blank-SAP to -4.4 ± 0.3 in SP-SAP (GLME p = 0.005). Evaluation windows were determined based on the duration of stimuli and the delayed onset of the hemodynamic response.

We further investigated single arterial dynamics during vibrissae stimulation with 2-photon microscopy. Following ablation of type-I nNOS neurons, after vibrissae stimulation there was a decrease in arteriole diameter (**Fig. 3e**) evaluated 3:7 seconds following stimulus onset from 11.6 ± 0.8 %·s in Blank-SAP (N = 9, 5M/4F, n = 81 arterioles) down to 7.8 ± 0.6 % in SP-SAP (N = 7, 2M/5F, n = 70 arterioles, GLME p = 0.008). The arterial changes closely mirror the Δ[HbT] changes, consistent with the substantial contribution of arterial dynamics to the blood volume signal (Huo, 2015). We also evaluated changes in blood volume during voluntary locomotion, where we saw a similar trend in decrease in locomotion-evoked Δ[HbT] evaluated 1.5:2.5 seconds following locomotion onset from 17.5 ± 2.0 µM in Blank-SAP (N = 7, 5M/2F) to 12.9 ± 2.0 µM in SP-SAP (N = 7, 2M/5F), but it was not statistically significant (GLME p = 0.10). These results show the removal of a very small number of neurons can drive substantial reductions in both hemodynamic and neural response to sensory stimulation.

Type-I nNOS ablation reduces low frequency neural activity

To determine the effect that type-I nNOS neuron removal had on neural activity, we assessed the power spectrum of the LFP in different arousal states, which we classified into alert, asleep, and all data (Turner, 2020). Data was classified into the alert state when 15-minute blocks were predominantly (> 80%) in the awake state. Alert periods contained fidgeting movements and bouts of whisking interspersed with awake quiescence. Periods classified as asleep were predominantly composed of sleeping states (NREM/REM > 80% of all classifications in a 15-minute block) with only brief periods of wakefulness, typically occurring during transitions between sleep states. The 'all' state includes everything irrespective of arousal state classification. The first ~60 minutes of each recording

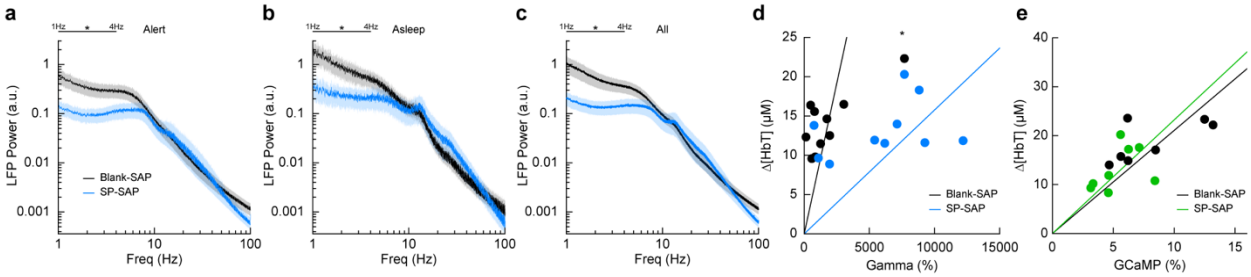

Figure 4. Type-I nNOS ablation alters low frequency neural activity and gamma-band neurovascular coupling (a) Local field potential within the vibrissae representation of somatosensory cortex during periods of Alert. **(b)** Asleep. **(c)** All data. **(d)** Change in gamma-band power vs. Δ[HbT] following brief (0.1 seconds) vibrissae stimulation. **(e)** Change in GCaMP7s fluorescence vs. Δ[HbT] following prolonged (5 seconds) vibrissae stimulation. Error bars represent population averages ± SEM. All statistics were evaluated between the indicated intervals. *p < 0.05, **p < 0.01, ***p < 0.001, GLME (**a-c**), GLM (**d, e**).

207 session which included vibrissae stimulation was excluded. There was a pronounced reduction in the delta-band (1-
208 4 Hz) power of the LFP in all three arousal state catagories. The power in the delta-band of the LFP in Blank-SAP mice
209 (N = 9, 4M/5F) in the alert state (**Fig. 4a**) was $3.4\times10^{-10} \pm 1.0\times10^{-10}$ a.u. compared to $1.0\times10^{-10} \pm 3.0\times10^{-11}$ a.u. in the
210 SP-SAP mice (N = 9, 5M/4F, GLME $p = 0.011$). The power in the delta-band of the LFP in Blank-SAP mice (N = 7, 3M/4F)
211 in the asleep state (**Fig. 4b**) was (NREM + REM) was $8.5\times10^{-10} \pm 3.0\times10^{-10}$ a.u. compared to $2.4\times10^{-10} \pm 9.1\times10^{-11}$ a.u.
212 in the SP-SAP mice (N = 7, 4M/3F, GLME $p = 0.022$). The power in the delta-band of the LFP in Blank-SAP mice (N =
213 9, 4M/5F) averaged across all arousal states (**Fig. 4c**) was $5.2\times10^{-10} \pm 1.7\times10^{-10}$ a.u. compared to $1.5\times10^{-10} \pm 4.3\times10^{-11}$
214 a. u. in the SP-SAP mice (N = 9, 5M/4F, GLME $p = 0.016$). These result parallel those seen in studies where knockout
215 of nNOS produces lower delta band power (Morairty, 2013) and optogenetic stimulation of nNOS neurons produces
216 low frequency oscillations (Zielinski, 2019), suggesting that type-I nNOS neurons promote these slow oscillations via
217 NO release. In contrast to the observed reductions in LFP, we noted no gross changes in the power spectra of cerebral
218 blood volume fluctuations between groups during any arousal state (**Fig. S4**).
219 We next wanted to see whether the amount of neural activity and corresponding Δ[HbT] in response to vibrissae
220 stimulation was altered following type-I nNOS neuron ablation. As a measure of neurovascular coupling, we used
221 the slope of the line fitting the change in gamma-band power vs. Δ[HbT] following brief (0.1 second) vibrissae
222 stimulation (**Fig. 4d**). Decreases in the slope indicate a smaller vascular response for a given amount of neural
223 activity, indicating a decrease in neurovascular coupling. We found the slope was significantly increased in SP-SAP
224 mice compared to Blank-SAP mice (Blank-SAP: 0.02 ± 0.03; SP: 0.005 ± 0.006, GLM $p = 0.0001$). We also evaluated
225 the change in GCaMP7s fluorescence vs. Δ[HbT] during prolonged (5 seconds) vibrissae stimulation from 2:5 seconds
226 (**Fig. 4e**) and saw no significant change in the slope (Blank-SAP: 251.3 ± 75.3; SP: 256.5 ± 73.2, GLM $p = 0.34$). Given
227 that the sensory-evoked LFP is driven more by synaptic input, while GCaMP7s signals are driven by local neural
228 activity, these results indicate that the loss of type-I nNOS neurons reduces overall excitability, but that the input
229 drive from other areas might be increased, potentially due to homeostatic mechanisms at the input synapses
230 (Turrigiano, 2008).

231 **Neurovascular coupling was weakly affected by type-I nNOS removal**

232 We next looked at the cross-correlation between blood volume and neural signals, which provides a measure
233 of spontaneous neurovascular coupling. For electrophysiological measures, we measured the cross-correlation
234 between gamma-band power and blood volume (**Fig. 5a**). We evaluated the peak cross-correlation during the
235 resting-state, during long periods while alert, or long periods while asleep. The cross-correlation between neural
236 activity and hemodynamic signals is substantially higher during periods of behavior (whisking, fidgeting) than during
237 the resting-state because self-generated motion and whisking drive increases in neural activity and vasodilation
238 (Winder, 2017; Drew, 2019b; Stringer, 2019; Claron, 2023; Tu, 2024) . The correlation between neural activity and
239 blood volume changes is higher during sleep than in the awake state (Turner, 2020). We saw no significant difference
240 in the peak cross-correlation during the resting-state (**Fig. 5b**) between Blank-SAP mice (N = 9, 4M/5F, 0.08 ± 0.007)

and SP-SAP mice (N = 9, 5M/4F, 0.06 ± 0.008, GLME p = 0.22). We did observe a significant difference in the peak cross-correlation during both periods of alert and asleep, from 0.23 ± 0.01 (Blank-SAP) to 0.16 ± 0.03 (SP-SAP, GLME p = 0.036) during alert periods (**Fig. 5c**) and 0.40 ± 0.02 (Blank-SAP) dropping to 0.33 ± 0.02 (SP-SAP, GLME p = 0.012) while asleep (**Fig. 5d**). We next wanted to evaluate whether this drop in neurovascular coupling was more prevalent at a particular modulation frequency. When analyzing the coherence between the gamma-band power and hemodynamic signals during these different arousal states, we noted no dominant frequency and saw no significant changes in the lower frequencies associated with neurovascular coupling (≤ 0.5 Hz). During the resting-state (**Fig. 5e**), the average coherence between 0.1 and 0.5 Hz was 0.28 ± 0.008 in Blank-SAP mice and 0.23 ± 0.01 in SP-SAP mice (GLME p = 0.23). The average coherence between 0.01 and 0.5 Hz during alert periods (**Fig. 5f**) was 0.29 ± 0.004 in Blank-SAP mice and 0.25 ± 0.005 in SP-SAP mice (GLME p = 0.06), and during asleep periods (**Fig. 5g**) it was 0.34 ± 0.008 in Blank-SAP mice and 0.32 ± 0.007 in SP-SAP mice (GLME p = 0.46). Lastly, to evaluate any changes in the predictive power of the neural-hemodynamic relationship, we fit a hemodynamic response function using the gamma-band power and hemodynamic response following periods of vibrissae stimulation. We observed that ablation of Type-I nNOS neurons did not alter the predictive power of the hemodynamic response function (**Fig. S5**).

We next evaluated neurovascular coupling from optical measures of bulk activity using GCaMP7s (**Fig. 5h**). The peak resting-state cross-correlation (**Fig.**

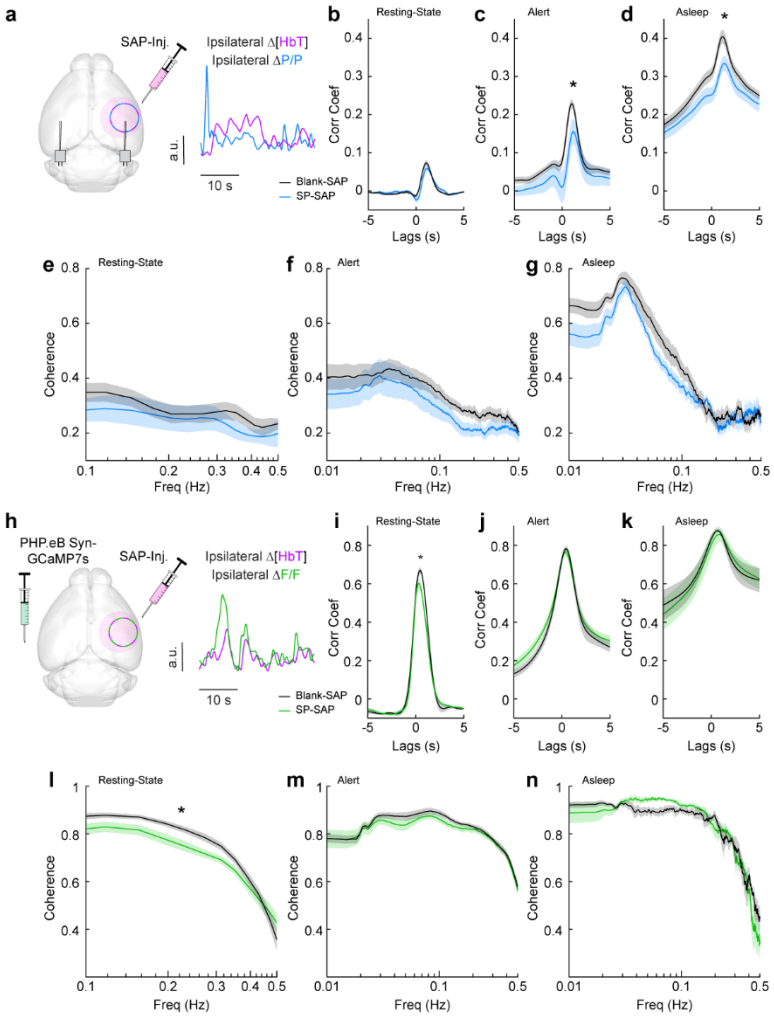

Figure 5. Neurovascular coupling was only weakly affected by type-I nNOS removal (a) Schematic demonstrating intracortical injection of either Blank-SAP or SP-SAP and the analysis of gamma-band power and hemodynamic signals from within the vibrissae representation of somatosensory cortex, N = 9 mice per group. **(b)** Gamma-Δ[HbT] resting-state cross-correlation **(c)** Gamma-Δ[HbT] alert cross-correlation **(d)** Gamma-Δ[HbT] asleep cross-correlation **(e)** Gamma-Δ[HbT] resting-state coherence **(f)** Gamma-Δ[HbT] alert coherence **(g)** Gamma-Δ[HbT] asleep coherence **(h)** Schematic demonstrating intracortical injection of either Blank-SAP or SP-SAP and the analysis of GCaMP7s fluorescence and hemodynamic signals from within the vibrissae cortex, n = 6-7 mice per group. **(i)** GCaMP7s-Δ[HbT] resting-state cross-correlation **(j)** GCaMP7s-Δ[HbT] alert cross-correlation (k) GCaMP7s-Δ[HbT] asleep cross-correlation **(l)** GCaMP7s-Δ[HbT] resting-state coherence **(m)** GCaMP7s-Δ[HbT] alert cross-correlation **(n)** GCaMP7s-Δ[HbT] asleep cross-correlation. Error bars represent population averages ± SEM. *p < 0.05, **p < 0.01, ***p < 0.001, GLME.

276 **5i**) between GCaMP7s fluorescence and ongoing hemodynamics showed a significant decrease, 0.68 ± 0.02 with
277 Blank-SAP versus 0.62 ± 0.02 with SP-SAP (GLME p = 0.038). However, there was no drop in peak cross-correlation
278 during either alert or asleep as seen with the gamma-band power. During alert periods (**Fig. 5j**), the peak GCaMP7s
279 cross-correlation was 0.78 ± 0.12 with Blank-SAP and 0.77 ± 0.02 with SP-SAP (GLME p = 0.54) while during asleep
280 periods (**Fig. 5k**) it was 0.88 ± 0.008 with Blank-SAP and 0.86 ± 0.04 with SP-SAP (GLME p = 0.58). Like the peak in
281 cross-correlation, the average resting-state coherence (**Fig. 5l**) did show a significant drop across the lower
282 frequencies, 0.75 ± 0.01 with Blank-SAP vs. 0.70 ± 0.01 with SP-SAP (GLME p = 0.049). There was no drop in coherence
283 during alert periods (**Fig. 5m**) at 0.78 ± 0.005 with Blank-SAP and 0.77 ± 0.004 with SP-SAP (GLME p = 0.42) nor during
284 asleep periods (**Fig. 5n**) at 0.75 ± 0.009 with Blank-SAP and 0.74 ± 0.01 with SP-SAP (GLME p = 0.63). While there are
285 small changes in neural-hemodynamic correlations, the differences in neurovascular coupling across arousal states
286 were relatively small following localized removal of type-I nNOS neurons, meaning any effects of ablation on
287 hemodynamic responses are primarily mediated by changes in neural activity.

Type-I nNOS ablation reduces low-frequency interhemispheric coherence

Because type-I nNOS neurons send and receive many modulatory signals across a range of distances, they could help serve to coordinate neural and vascular dynamics across the brain. We tested this hypothesis by comparing how loss of type-I nNOS neurons changed the coherences of neural and hemodynamics signals between the left and right vibrissae cortex, which are generally highly correlated across all behaviors and frequencies (Turner, 2020). Neural activity is also bilaterally correlated, though less so than vascular dynamics. Average resting-state coherence between the left and right Δ[HbT] signals (**Fig. 6a**) in the vibrissae cortex were 0.79 ± 0.005 for Blank-SAP and 0.73 ± 0.008 for SP-SAP mice (p = 0.014, GLME, **Fig. 6b**). This reduction in coherence was seen over all frequencies (0-0.5 Hz) during both alert periods (**Fig. 6c**), at 0.86 ± 0.002 for Blank-SAP and 0.81 ± 0.003 for SP-SAP ($p = 7.4\times10^{-6}$, GLME), as well as asleep periods (**Fig. 6d**) with 0.86 ± 0.003 for Blank-SAP and 0.79 ± 0.005 for SP-SAP (p = 0.0008, GLME).

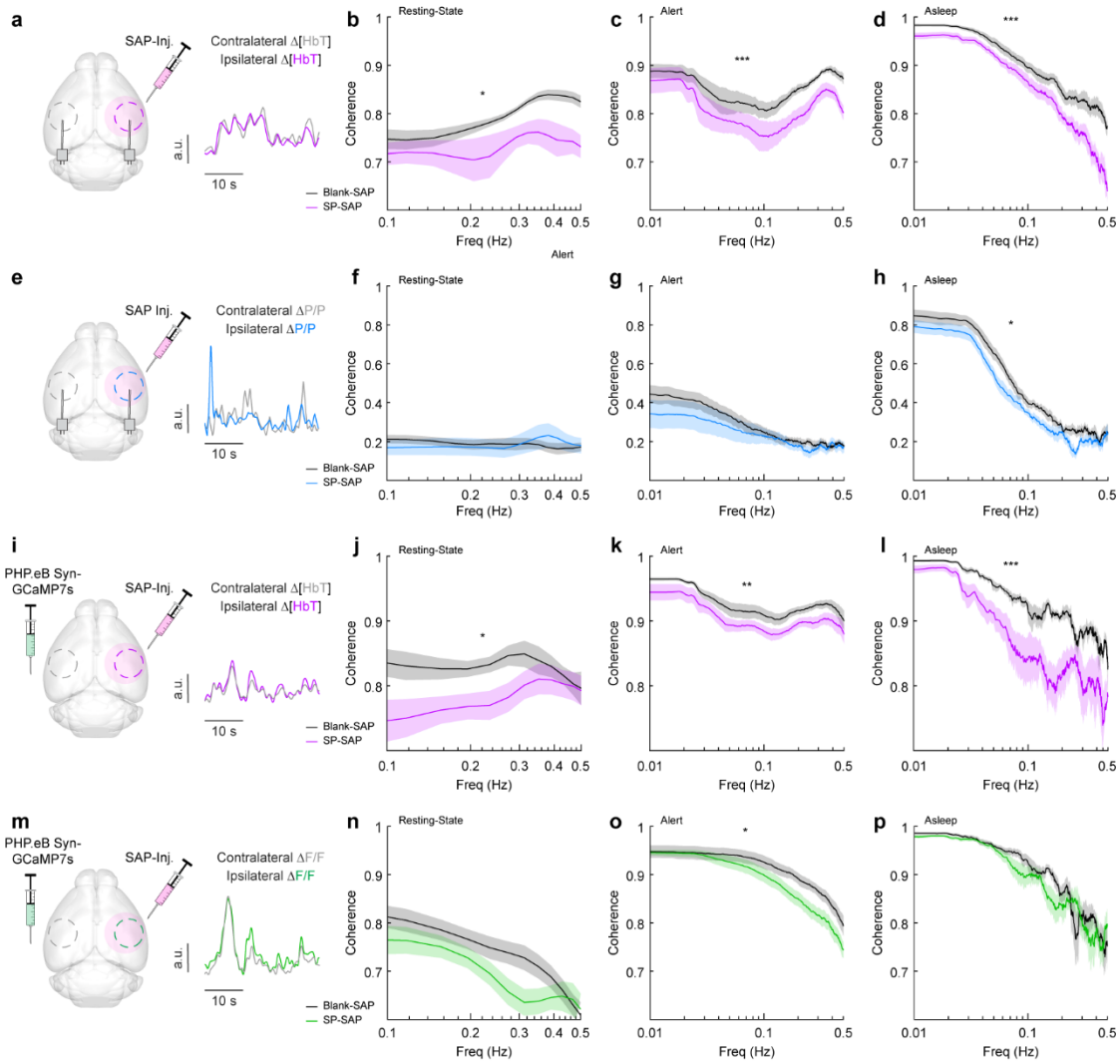

Figure 6. Type-I nNOS ablation reduces low-frequency interhemispheric coherence (a) Δ[HbT] coherence between bilateral ROIs in the left and right hemisphere's somatosensory cortex during **(b)** Res.t **(c)** Alert. **(d)** Asleep. **(e)** Gamma-band power coherence between bilateral ROIs in the left and right hemisphere's somatosensory cortex during **(f)** Res.t **(g)** Alert. **(h)** Asleep. **(i)** Δ[HbT] coherence between bilateral ROIs in the left and right hemisphere's somatosensory cortex during **(j)** Res.t **(k)** Alert. **(l)** Asleep. **(m)** GCaMP7s coherence between bilateral ROIs in the left and right hemisphere's somatosensory cortex during **(n)** Res.t **(o)** Alert. **(p)** Asleep. Error bars represent population averages ± SEM. *p < 0.05, **p < 0.01, ***p < 0.001, GLME.

We then looked at the coherence of gamma-band power across hemispheres, where average coherence for bilateral gamma-band signals in the resting-state were 0.19 ± 0.006 (Blank-SAP) and 0.19 ± 0.01 (SP-SAP, p = 0.88, GLME, **Fig 6e, f**). There was no significant difference during the alert periods (**Fig 6g**) at 0.22 ± 0.005 (Blank-SAP) and 0.20 ± 0.006 (SP-SAP, p = 0.43, GLME), but ablation of type-I nNOS neuros produced a reduction of coherence during asleep periods (**Fig. 6h**) at 0.35 ± 0.009 (Blank-SAP) and 0.29 ± 0.009 (SP-SAP, p = 0.047, GLME).

Average resting-state coherence across bilateral Δ[HbT] signals (**Fig. 6i**) taken from the vibrissae cortex were 0.83 ± 0.005 (Blank-SAP) and 0.78 ± 0.007 (SP-SAP, p = 0.021, GLME, **Fig. 6j**). This reduction in coherence persisted across all frequencies during the both alert periods (**Fig. 6k**) at 0.92 ± 0.001 (Blank-SAP) and 0.90 ± 0.001 (SP-SAP, p = 0.012, GLME) as well as sleep periods (**Fig. 6l**) at 0.90 ± 0.002 (Blank-SAP) and 0.83 ± 0.005 (SP-SAP, p = 0.004, GLME). Average resting-state coherence across bilateral GCaMP7s signals (**Fig. 6m**) taken from the vibrissae cortex were 0.75 ± 0.009 (Blank-SAP) and 0.70 ± 0.009 (SP-SAP, GLME p = 0.12, **Fig. 6n**). This reduction in coherence persisted across all frequencies during the both alert periods (**Fig. 6o**) at 0.88 ± 0.003 (Blank-SAP) and 0.84 ± 0.003 (SP-SAP, p = 0.029, GLME) but not in sleep periods (**Fig. 6p**) at 0.85 ± 0.005 (Blank-SAP) and 0.84 ± 0.005 (SP-SAP, GLME p = 0.52). When the correlation of bilateral signals was evaluated with Pearson's correlation coefficients, the same general trend remained (**Fig. S6**). These results show that removal of type-I nNOS neurons reduces both vascular and neural coordination across hemispheres.

Type-I nNOS neurons control vasomotion amplitude but not baseline diameter

We next wanted to establish how ablation of type-I nNOS neurons affected vasomotion, spontaneous oscillations in the absence of behavior, measured at the scale of blood volume and at the level of single arterioles, as well as the basal tone of blood vessels. The variance in Δ[HbT] during rest, a measure of vasomotion amplitude, was significantly reduced following type-I nNOS ablation (**Fig. 7a**), dropping from 40.9 ± 3.4 μM^2 in the Blank-SAP group (N = 24, 12M/12F) to 23.3 ± 2.3 μM^2 in the SP-SAP group (N = 24, 11M/13F) (GLME $p = 6.9\times10^{-5}$). Individual pial and penetrating arterioles showed the same reduction in vasomotion after type-I nNOS neuron ablation, with Blank-SAP (N = 9, 5M/4F, n = 70 arterioles) having a resting diameter variance of 12.6 ± 1.4 $\%^2$ and SP-SAP (N = 7, 2M/5F, n = 65 arterioles) of 8.0 ± 0.8 $\%^2$ (**Fig. 7b**).

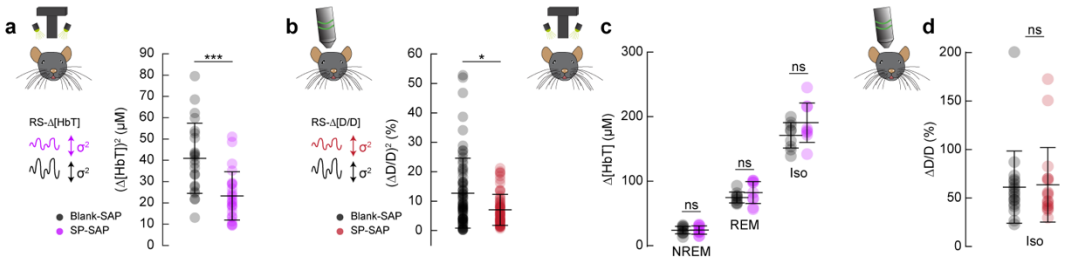

Figure 7. Type-I nNOS ablation reduces resting-state hemodynamics and low frequency neural activity (a) Variance in resting-state hemodynamics signals measured with widefield optical imaging. **(b)** Variance in resting-state arteriole diameter measured with two-photon. **(c)** Average Δ[HbT] during periods of NREM sleep, periods of REM sleep, and following administration of isoflurane (n = 9 mice per group). **(d)** Change in normalized arteriole diameter following administration of isoflurane Error bars represent population averages ± SD. All statistics were evaluated between the indicated intervals. *p < 0.05, **p < 0.01, ***p < 0.001 GLME.

323 If type-I nNOS neurons control the basal diameter of vessels via secreted vasodilators, potentially in an arousal
324 state dependent way, when we ablate these neurons we would observe a difference in blood volume across arousal
325 states and in the maximal dilation elicited with isoflurane (Gao, 2015). We saw no changes in the average change in
326 Δ[HbT] across states (**Fig. 7c**, **Fig. S7**). The resting-state Δ[HbT] in Blank-SAP mice was 0.29 ± 0.7 μM compared to
327 0.29 ± 0.9 μM in SP-SAP (GLME p = 0.997). NREM Δ[HbT] in Blank-SAP mice was 23.9 ± 5.8 μM compared to 24.1 ±
328 6.5 μM in SP-SAP (GLME p = 0.96). REM Δ[HbT] in Blank-SAP mice was 74.5 ± 8.4 μM compared to 82.3 ± 17 μM in
329 SP-SAP (GLME p = 0.26). The Δ[HbT] following isoflurane in Blank-SAP mice was 170.9 ± 19.7 μM compared to 190.5
330 ± 30.5 μM in SP-SAP (GLME p = 0.15). We repeated the isoflurane experiment on a set of pial and penetrating
331 arterioles under 2-photon microscopy. The change in normalized arteriole diameter following administration of
332 isoflurane (n = 7-9 mice per group, 18-19 arterioles per group) was 61 ± 37.2% in Blank-SAP compared with 63.6 ±
333 38.4% in SP-SAP (p = 0.85, ttest). These results indicate that type-I nNOS neurons play a role in driving spontaneous
334 hemodynamic fluctuations, but not in setting the basal diameter during different states.

335 **Discussion**

336 We selectively ablated type-I nNOS neurons from the somatosensory cortex, which had marked effects on
337 neural activity and vascular dynamics, but minimal changes in neurovascular coupling. These results are surprising
338 given previous work showing stimulation of these neurons in isolation causes vasodilation and minimal neural
339 activity changes. Our approach of using SP-conjugated saporin allowed a nongenetic means of targeting a critical
340 neuronal cell type, supporting further exploration of the role of type-I nNOS neurons in transgenic mouse models of
341 disease without complicated breeding schemes, as well as in non-model organisms. Our results point to these
342 neurons being an important orchestrator of neural and vascular dynamics, as loss of these neurons causes
343 desynchronization between hemispheres of both neural and vascular signals, as well as altered responses to sensory
344 stimulation. While previous studies using specific activation of type-I nNOS neurons have emphasized the roles of
345 these neurons in driving vasodilation with minimal changes in neural activity, our results point to a larger role of
346 these neurons in organizing and patterning both spontaneous and sensory-evoked neural activity. This is likely due
347 to a loss in NO signaling as well as a loss of the many of the other neuropeptides expressed by type-I nNOS neurons,
348 which all have known effects on other neurons.

349 While previous studies have found that activation of type-I nNOS neurons, either optogenetically or via
350 administration of substance P, results in vasodilation (which would imply an important role for these neurons for
351 neurovascular coupling), our work provides insight into the integrated function of type-I nNOS neurons in neural
352 circuits and vascular dynamics. Importantly, methodological approaches differentiate our strategy from previous
353 published work. One interpretation is that there could be compensatory rewiring of local and/or network activity
354 following type-I nNOS ablation, where other signaling pathways from the neurons to the vasculature become
355 strengthened to compensate for the loss of vasodilatory signaling from the type-I nNOS neurons. While this likely
356 happens to some degree, this interpretation is less likely to completely account for the effect given these potential

357 compensatory changes do not prevent large changes in neural activity and resting vasomotion. Second, there may
358 be some non-linear interactions between vasodilatory signals and/or the vasodilator mechanisms that are arousal-
359 state-dependent. The diameter of arteries tracks the smooth muscle membrane potential linearly, up until a
360 saturation point above which any hyperpolarization does not induce further dilation (Knot, 1998; Wölfle, 2011; Hill,
361 2012). Many vasoactive pathways from neurons to vessels are known to exist, whose additive individual effects could
362 account for larger than biologically possible changes in vasodilation (Hosford, 2019). It may be that for dilation
363 occurring during sensory stimulation and sleep, the vasodilatory stimulus to vessels exceeds the saturation point, so
364 that the loss of one vasodilatory pathway does not further affect the vascular response (**Fig. S8**). This would also be
365 consistent with isolated optogenetic or chemical stimulation of type-I nNOS neurons being able to drive substantial
366 dilation, while the loss of these neurons does not have a large impact on the vascular response.

367 Finally, pharmacological ablation and optogenetic/chemogenetic activation are not mirror manipulations and
368 have differences that can produce non-symmetrical changes. Symmetrical changes would only occur if the neural
369 circuitry and the signaling to the vessel were completely linear. Optogenetic activation/deactivation of a single cell
370 type does not produce symmetrical changes in the activity of other neurons (Phillips, 2016), so there is little reason
371 to think ablation would have the exact opposite effect as activation. Furthermore, optogenetic/pharmacological
372 activation of a single cell type is unlikely to occur endogenously, as neural activity across different cell types is largely
373 correlated (Bugeon, 2022). For example, during whisker stimulation, not only are type-I nNOS neurons in the
374 somatosensory cortex activated (Ruff, 2024), but nearly every other cell type is as well (Staiger, 2021), which mean
375 that type-I nNOS neurons are not the only neurons, and not even the only NO producing neurons, sending signals to
376 the vasculature during sensory stimulation.

377 One surprise is that we observed no changes in the vasodilation during NREM sleep, where type-I nNOS neurons
378 are known to be active and play a role in inducing sleep (Kilduff, 2011). During NREM sleep, there is marked arterial
379 dilation (Turner, 2020; Gheres, 2023), and it would seem natural that type-I nNOS neurons might drive this. However,
380 we saw no difference in NREM dilation between the ablated and control mice. Again, this could be due to
381 compensation, saturation of the vasodilatory response, or it could be due to type-I nNOS neurons releasing other
382 vasoconstrictory peptides (SST, NPY) so their net effects are cancelled out. This last possibility is consistent with the
383 loss of the post-stimulus vasoconstriction seen after type-I nNOS neuron ablation. Again, like with sensory
384 stimulation, there may be a non-linearity in the vascular responses, so that another large factor, such as large
385 neuromodulatory changes during sleep, could dominate over any other vascular signaling factor. The large
386 norepinephrine decreases during NREM (Osorio-Forero, 2021; Kjaerby, 2022; Turner, 2023) could release the vessels
387 from tonic vasoconstriction (as norepinephrine is a vasoconstrictor (Bekar, 2012)), resulting in the dilation during
388 NREM.

389 Finally, we saw a marked reduction in spontaneous vascular oscillation (vasomotion) at rest, both at the level of
390 single arteries, and at the level of blood volume. These spontaneous oscillations move cerebrospinal fluid (CSF) (van
391 Veluw, 2020; Kedarasetti, 2022; Holstein-Ronsbo, 2023) which is important for clearing waste from the brain, and a

392 reduction in amplitude will decrease the pumping efficacy. Additionally, there is a loss of coordination of neural and
393 vascular dynamics across hemispheres after ablation of type-I nNOS neurons, indicated by the drop in coherence.
394 Although a loss of synchronous dilations/constrictions might affect CSF movement, we might imagine that it would
395 also adversely impact CSF pumping. Aged human brains show reduced interhemispheric synchrony in resting-state
396 signals (Zhao, 2020), analogous to what we see here. Type-I nNOS neurons also seem uniquely vulnerable to stress
397 (Han, 2019), and loss of type-I nNOS neurons reduces power in the 1-4Hz band of the LFP, which is positively
398 associated with CSF clearance (Hablitz, 2019; Jiang-Xie, 2024). It is possible that adverse life experiences could cause
399 the loss of type-I nNOS neurons, leading to reduction in CSF flow seen in age (Kress, 2014; Matrongolo, 2023) that is
400 thought to correlate with neurodegeneration.

401 **Materials and Methods**

402 This study was performed in accordance with the recommendations of the Guide for the Care and Use of
403 Laboratory Animals of the National Institutes of Health. All procedures were performed in accordance with protocols
404 approved by the Institutional Animal Care and Use Committee of Pennsylvania State University (Protocol
405 201042827). Data were acquired from 119 C57BL6/J mice (#000664, The Jackson Laboratory, Bar Harbor, ME)
406 compromised of 57 males and 62 females between 3 and 9 months of age. Food and water were provided *ad libitum*
407 and animals were housed on a 12-hr. light/dark cycle with all experiments occurring during the light cycle. Mice were
408 individually housed after surgery. Sample sizes are consistent with previous studies (Winder, 2017; Turner, 2020;
409 Turner, 2023) and experimenters were not blind to experimental conditions or data analysis except for histological
410 experiments.

411 **Surgical Procedures.** Saporin is a ribosome-inactivating protein that was conjugated to the Sar^9, $Met(O_2)^{11}$ analog of
412 Substance P (SP-SAP) or to a control peptide (Blank-SAP) (IT11 & IT21, Advanced Targeting Systems, Carlsbad, CA).
413 Mice were anesthetized using 5% isoflurane (2% maintenance) vaporized in pure oxygen and were then injected
414 intracortically with 4 ng of either SAP conjugate or Blank-SAP in 100 nL of artificial cerebrospinal fluid (aCSF). The
415 incision site was sterilized with betadine and 70% ethanol followed by a retraction of the skin atop the skull. A small
416 (< 0.5 mm) craniotomy was made above the vibrissae representation of somatosensory cortex (2 mm caudal, 3.25
417 mm lateral) and a sterile glass-pulled needle (tip diameter 50-100 µm) was inserted 500 µm beneath the cortical
418 surface at 45°. The SAP conjugate was slowly injected at 100 nL/min using a programmable syringe pump (Harvard
419 Apparatus, Holliston, MA) followed by closure of the incision with VetBond (3M, Saint Paul, MN). A subset of animals
420 were also injected retro-orbitally with 25 µL of AAV PHP.eB-syn-jGCaMP7s-WPRE [$2x10^{13}$ GC/mL] (104487-PHPeB,
421 Addgene, Watertown, MA) diluted in 25 µL of sterile saline. Animals were given at least 2 weeks to recover prior to
422 undergoing additional procedures. For imaging, a custom-machined titanium head bar was adhered atop the
423 occipital bone of the skull using cyanoacrylate glue (Vibra-Tite 32402, ND Industries, Clawson, MI) and dental cement
424 (Ortho-Jet, Lang Dental, Wheeling, IL). Self-tapping 3/32' #000 screws (J.I. Morris, Oxford, MA) were implanted in
425 the frontal bones for structural stability. Electrodes were implanted into cortex and hippocampus using PFA-coated

426 tungsten stereotrodes (#795500, AM systems, Sequim, WA) for recordings of local field potentials (LFP) and into the
427 neck muscles using a pair of PFA-coated 7-strand stainless-steel wires (#793200, AM systems, Sequim, WA) for
428 electromyography (EMG). Polished and reinforced thinned-skull windows (Drew et al., 2010a; Shih et al., 2012b)
429 were implanted over the somatosensory areas (either bilaterally or right hemisphere) using #0 coverslips (#72198,
430 Electron Microscopy Sciences, Hatfield, PA). Detailed surgical procedures are as previously described (Turner, 2020).

431 **Data acquisition.** Data were acquired with a custom LabVIEW program (National Instruments;
432 https://github.com/DrewLab/ LabVIEW-DAQ). Details on widefield optical imaging, electromyography (EMG),
433 electrophysiology, vibrissae stimulation, and behavioral measurements including tracking of vibrissae and pupil
434 diameter were performed as previously described (Turner, 2020; Zhang, 2022; Turner, 2023)). Mice were gradually
435 acclimated to head-fixation of increasing duration (15, 30, 60 minutes) on the days preceding the onset of
436 experiments. The vibrissae (left, right, or a third air puffer not directed at the body as an auditory control) were
437 randomly stimulated with air puffs [0.1 seconds or a train of 5 second pulses, 10 pounds force per square inch (PSI)]
438 occurring every 30–45 seconds for the first 1 hour of imaging. Data were acquired in 15-minute intervals with a brief
439 (~30 seconds) gap in between for saving data to disk. Each animal was run for up to 6 imaging sessions lasting from
440 1-5 hours depending on experiment.

441 **Histology.** Following the conclusion of imaging experiments, animals were deeply anesthetized and transcardially
442 perfused with heparin-saline followed by 4% paraformaldehyde. Presence or absence of nNOS-positive neurons in
443 the injected hemisphere was verified using nicotinamide adenine dinucleotide phosphate (NADPH)-diaphorase
444 staining for localizing the sparsely populated type-I nNOS neurons (Scherer-Singler, 1983).

445 **Immunohistochemistry.** All histological analyses were done blinded to the experimental condition. Mice were
446 deeply anesthetized with 5% isoflurane and perfused transcardially with ice-cold phosphate buffered saline (PBS, pH
447 7.4) and 4% paraformaldehyde (PFA, pH 7.4). Brains were removed, post-fixed in PFA for 24 hours and stored in PBS
448 at 4°C for less than 1 week. A fiduciary mark was placed in the right hemisphere. 40-µm free floating sections were
449 sliced with a Leica vibratome (VS 1200, Leica) and stored in PBS for less than 1 week. Prior to immunostaining, slices
450 were washed three times in PBS for 10 minutes each, and underwent antigen retrieval in 10 mM sodium citrate
451 buffer (pH 6.0) at 80°C for 30 minutes. Slices were washed three times in PBS for 10 minutes each, and permeabilized
452 in 0.5% Triton X-100 in PBS for 60 minutes. Nonspecific binding was blocked with 5% normal donkey serum (NDS)
453 (ab7475) in 0.1% Triton X-100 in PBS for 60 minutes. Slices were then incubated in a primary antibody cocktail,
454 including goat anti-nNOS (1:500, ab1376), rabbit anti-IBA-1 (1:500, ab178847), rat anti-GFAP (1:500, Thermofisher
455 13-0300), rabbit anti NeuN (1:2000, EnCor), rabbit anti-TACR1 (1:500 Invitrogen PA1-16713) in 2.5% NDS in 0.1%
456 Triton X-100 in PBS for 48-h at 4°C. Slices were rinsed three times with PBS for 10 minutes each, and incubated in a
457 fluorophore-tagged secondary antibody cocktail, including donkey anti-rabbit Alexa Fluor 488 (1:500, ab150073),
458 donkey anti-goat Alexa Fluor 594 (1:500, ab150132), donkey anti rabbit Alexa fluor 647 (1:500, ab150075), donkey

459 anti rat Alexa fluor 488 (1:500 ab150153), for 4 hours at room temperature. Slices were rinsed again three times
460 with PBS, with the last step including DAPI (1:10,000, 10mg/mL, Millpore Sigma, 10236276001), mounted on glass
461 slides, air-dried and cover slipped with Immunomount (Thermo Fisher Scientific, Waltham, MA, United States).
462 Images were obtained with an Olympus BX63 upright microscope (Center Valley, PA, United States) under matched
463 exposure settings. Three to eight images from both hemispheres were taken per region.

464 **Cell counting and immunofluorescence quantification.** Total cell counts and absolute changes in
465 immunofluorescence (**Fig. 1**) were quantified using ImageJ (National Institutes of Health, Bethesda, MD, United
466 States). For total cell counts, a region of interest (ROI) was delineated, and cells were automatically quantified under
467 matched criteria for size, circularity and intensity. Each ROI's total cell count was divided by the ROI's area to give a
468 total density value (Dao, 2020; Smith, 2020; Sicher, 2023). Immunoreactivity was quantified as mean fluorescence
469 intensity of the ROI (Pleil, 2015).
470
471 **Data Analysis.** Data were analyzed with code written by K.L.T, M.S.H, Q.Z, K.W.G, and P.J.D. (MATLAB 2019b–2024a,
472 MathWorks).

473 **Statistical analysis.** Statistical evaluations were made using either generalized linear mixed effects (GLME), unpaired
474 t-test, or general linear model (GLM). GLME models had the arousal state as a fixed effect, mouse identity as a
475 random effect, and hemisphere [left/right (L/R), if applicable] as an interaction with the animal ID, or using a paired
476 t test where appropriate. Unless otherwise stated, statistical results report p values from a GLME test. All reported
477 quantifications are mean ± SD unless otherwise indicated. Unless otherwise noted, all pupil diameter measurements
478 are in z-units. MATLAB functions used were fitglme, ttest, fitglm.

479 **Hemodynamic correction.** Widefield imaging was done with a Dalsa 1M60 Pantera CCD camera (Phase One,
480 Cambridge, MA) with a magnifying lens (VZM 300i, Edmund Optics, Barrington, NJ). Reflectance measurements (**Fig.**
481 **2**) were converted to changes in total hemoglobin (Δ[HbT]), oxy-hemoglobin (Δ[HbO]), and deoxy-hemoglobin
482 (Δ[HbR]) using the Beer–Lambert law (Ma et al., 2016a, b). Correction for attenuation of GCaMP7s fluorescence due
483 to absorption of the surrounding tissue was corrected as previously described (Kramer, 1979; Ma, 2016b; Wright,
484 2017; Scott, 2018). Changes in fluorescence intensity in the GCaMP7s signal due to blood absorption were
485 approximated in a pixel-wise fashion by multiplying each value by the ratio of the green and blue channel's resting
486 baseline pixel value.

487 **Electrophysiology.** Gamma-band [30–100Hz] LFP band was digitally bandpass filtered from recorded broadband
488 data using a third-order Butterworth filter, squared, low-pass filtered below 1 Hz, and resampled at 30 Hz. Time-
489 frequency spectrograms (**Fig. 2**) were calculated using the Chronux toolbox version 2.12 v03 (Bokil, 2010), function
490 mtspecgramc with a 5 s window and 1/5 s step size using [5,9] tapers and a passband of 1–100 Hz to encompass the

LFP. EMG (300–3 kHz) from the neck muscles was bandpass filtered, squared, convolved with a Gaussian kernel with a standard deviation of 0.5 seconds, log transformed, then resampled at 30 Hz. MATLAB function(s): butter, zp2sos, filtfilt, gausswin, log10, conv, resample.

Evoked responses and slope. Evoked responses (**Fig. 3**) including whisker stimulation and locomotion for the various data types ([HbT], [HbO], [HbR], GCaMP7s, arteriole diameter) were compared between the indicated intervals (i.e., 2:4 seconds post-stimulation). The mean of the 2 seconds preceding event onsets were subtracted from the event and smoothed with a 3rd order Savitzky-Golay filter. The average slope was calculated by comparing the rise (Δ[HbT]) over the run (neural data) before being fit with a linear model forced through the origin. MATLAB function(s): sgolayfilt)

Spectral power and coherence. Spectral power (**Fig. 4, 5, 6 S5**) was estimated using the Chronux toolbox (Bokil, 2010) function mtspectrumc. Data was detrended within individual events and truncated to the desired length depending on behavior (10 seconds for rest, 15 minutes for Alert and Asleep). Coherence analysis between two signals within the same hemisphere or between signals recorded bilaterally was run for each data type Chronux function coherencyc after detrending using the MATLAB function detrend.

Cross-correlation. Cross-correlations (**Fig. 5**) between gamma-band power or ΔF/F and changes in total hemoglobin Δ[HbT] were taken during periods of resting-state, alert, and asleep. Data were mean-subtracted and digitally lowpass filtered (< 1 Hz) with a fourth-order Butterworth filter (MATLAB function(s): butter, zp2sos, filtfilt). Cross-correlation analysis was run for each arousal state (MATLAB function(s): xcorr) with a ± 5 second lag time.

Resting-state variance and Δ[HbT] during different arousal states. Variance during the resting-state for both Δ[HbT] and diameter signals (**Fig. 7**) was taken from resting-state events lasting ≥10 seconds in duration. Average Δ[HbT] in each arousal state was taken with respect to awake resting baseline events ≥10 seconds in duration. Continuous NREM sleep events ≥30 seconds, REM sleep events ≥60 seconds, and periods following administration of isoflurane were compared between groups. Each event was digitally lowpass filtered (<1 Hz) with a fourth-order Butterworth filter (MATLAB function(s): butter, zp2sos, filtfilt) and then averaged within each individual time series prior to comparing across animals/groups.

Open field behavior. Exploratory behavior (**Fig. S2)** was measured in a custom-made 30 cm x 60 cm arena during the light phase. Mice were not habituated to the arena. Mice were placed in the arena for 10 minutes to explore, and their behavior was recorded using an overhead camera (Blackfly BFLY-U3-23S6M, Teledyne FLIR, Wilsonville, OR) with 6 mm fixed focal length lens (Edmund Optics, Barrington, NJ, Stock #33939) at a frame rate of either 15 or 30 frames per second. The arena was illuminated with 780nm light. The surroundings of the arena were dark during the entire recording session. The arena was cleaned with 70% ethanol in between animals. Only the first 5 minutes

523 of the behavior were analyzed and reported here. The total distance traveled over the first 5 minutes and the time
524 spent in the 25 x 55 cm center rectangle were quantified. Generalized linear mixed effect (GLME) was used in
525 MATLAB to perform statistical analysis. No statistical outliers were removed from the data. Mouse behavior was
526 tracked using DeepLabCut (Mathis, 2018) and analyzed with custom MATLAB algorithms (Zhang, 2022; Brockway,
527 2023). Eight points on the body (left ear, right ear, head, mid, back near the hip joint, base of the tail, midpoint of
528 the tail, and end of the tail) were tracked. Four markers placed in the arena's four corners with an additional four
529 points calculated from the four corners to track the center rectangle. A DeepLabCut model was trained and
530 evaluated on a subset of mice before applying the model to all the mice. DeepLabCut tracking was considered
531 acceptable if the tracking confidence was above 97%; however, in most cases, it was higher than 99%. Tracking
532 positions were exported to a CSV file containing the tracked location's XY coordinates (frame pixels). Tracked videos
533 from random mice were visualized to confirm the accuracy of the tracking. The experimenter was blinded to drug
534 injection group identification until tracking and analysis were completed. The distance was calculated from the first
535 5 minutes as Euclidean distance between the point tracked in the middle of the mouse body from subsequent
536 frames. Center time was quantified as the number of frames a mouse spends within the polygon bounded by 4 points
537 tracked on the center of the arena.

538 **Sleep scoring.** Sleep scoring (**Fig. S3**) was performed as in Turner et al. (2020). Briefly, arousal state was scored using
539 a combination of cortical and hippocampal LFP, EMG, pupil diameter, and whisker and body moment. Periods of
540 manually-chosen awake rest 5s in duration with no vibrissae motion, and no body motion were used as a baseline
541 to normalize neural and hemodynamic signals. NREM sleep shows elevated cortical delta-band power and lower
542 EMG power. REM sleep is marked by elevated hippocampal theta-band power and elevated cortical gamma-band
543 power with very low baseline EMG power (muscle atonia; Cantero et al., 2004; Montgomery et al., 2008; Le Van
544 Quyen et al., 2010; Sullivan et al., 2014). Every 5 second interval was classified as either Awake, NREM sleep, or REM
545 sleep using a bootstrap aggregating random forest model with the predictors of cortical delta band power, cortical
546 beta band power, cortical gamma LFP, hippocampal theta LFP, EMG power, heart rate, and whisking duration. Sleep
547 model accuracy was validated using the out-of-bag error during model training. MATLAB functions used were
548 TreeBagger, oobError, predict.

549 **Pupil diameter and interblink interval.** Pupil diameter (**Fig. S2**) was lowpass filtered at 1 Hz with a fourth-order
550 Butterworth filter. Changes in whisking-evoked and stimulus-evoked (contralateral, auditory) diameters normalized
551 relative to the mean of the 2 second preceding the event onset. MATLAB functions used were butter, zp2sos, filtfilt.
552 Interblink interval and blink-associated physiology. Because of breaks in recording to save the data to disk, interblink
553 interval was calculated between blinks occurring within 15 min records and not blinks on the edges of trials. Blinks
554 that occurred within 1 second of each other were linked together as blinking bouts, and all blink-triggered analyses
555 were with respect to the first blink in a series. Blink-triggered averages were separated into two groups depending

556 on the arousal state classification of the 5 second bin before the blink, being either Awake (arousal state classification
557 of Awake) or Asleep (arousal state classification being either NREM or REM).

558 **Hemodynamic response function.** The hemodynamic response function (HRF, **Fig. S5**) was calculated as previously
559 described (Winder, 2017; Zhang, 2023) using both deconvolution and fitting the response to a gamma distribution.
560 Only neural activity (gamma-band power, 30-100 Hz) within 1.5 second of the stimulus was used for calculating the
561 HRF. Each HRF was calculated using half of the data and tested on the other half. To test the predictive capability of
562 each HRF, the impulse function was fit with a gamma-distribution function and convolved with the neural power to
563 predict the measured hemodynamic signal. The coefficient of determination (R^2) between the predicted and actual
564 hemodynamic signal was evaluated to quantify the efficacy of HRF's prediction (MATLAB function(s): sgolayfilt,
565 detrend, fminsearch, fitlm).

566 **Pearson's correlation coefficient calculations.** The Pearson's correlation coefficient between bilateral signals (**Fig.**
567 **S6**) was obtained by mean-subtracting and digitally lowpass filtering (<1 Hz) with a fourth-order Butterworth filter
568 and then taking the Pearson's correlation coefficient (MATLAB function(s): butter, zp2sos, filtfilt, corrcoef).

569 **Arousal state transitions.** Transitions between arousal states (Awake to NREM, NREM to Awaken, NREM to REM,
570 REM to Awake) were compared across groups (**Fig. S7**) by averaging events that met the criteria of 30 seconds of
571 one state's consecutive classifications followed by 30 seconds of another state. The difference in the Δ[HbT] between
572 the pre- and post- state transition were compared by taking the 30:10 seconds prior to the transition zero point to
573 the 10:30 seconds following. [HbT] was digitally lowpass (<1 Hz) filtered using a fourth-order Butterworth filter
574 (MATLAB function(s): butter, zp2sos, filtfilt).

575 **Data availability.** Data and code for generating the figures are available at [pending Dryad link once Manuscript
576 number is assigned] and analysis code is available at https://github.com/KL-Turner/Turner-nNOS-Manuscript. Raw
577 data is available upon reasonable request.

578 **Supplemental Figure 1**

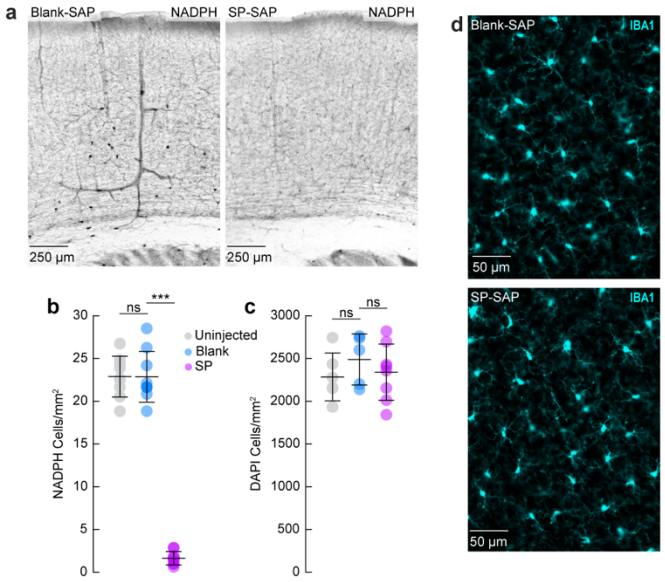

Figure S1. Histological quantification of cortical SP-Sap injections (a) Examples of NADPH diaphorase staining fromBlank-SAP and SP-SAP injected mice. **(b)** SP-SAP injected mice (N = 9, 5M/4F) had significantly lower numbers of type-I nNOS cells than either Blank-SAP (N = 9, 4M/5F) or Uninjected mice (N = 9, 4M/5F) (SP-SAP: 1.6 ± 0.8 neurons/mm^2; Blank-SAP: 22.9 ± 2.4 neurons/mm^2; Uninjected: 22.9 ± 3 neurons/mm^2; Blank-SAP vs. Uninjected: p = 0.98; Blank-SAP vs. SP-SAP: p = 2.23×10^{-13}). **(c)** Counts of DAPI-labeled cell nuclei per square mm from imaged mice. Uninjected (N = 6, 6M) mice had 2284 ± 279 DAPI-labeled cell bodies/mm^2, which was not significantly different than those injected with Blank-SAP (N = 5, 5F, 2488 ± 298, *p* = 0.23, GLME), which in turn was not significantly different than those injected with SP-SAP (N = 8, 4M/4F, 2340 ± 329, *p* = 0.39, GLME. **(d)** Representative image of IBA1 for Blank-SAP (top) and SP-SAP (bottom) taken from **Fig 1c**. Error bars (**b, c**) denote SD. *α < 0.05, **α < 0.01, ***α < 0.001, GLME.

579 **Supplemental Figure 2**

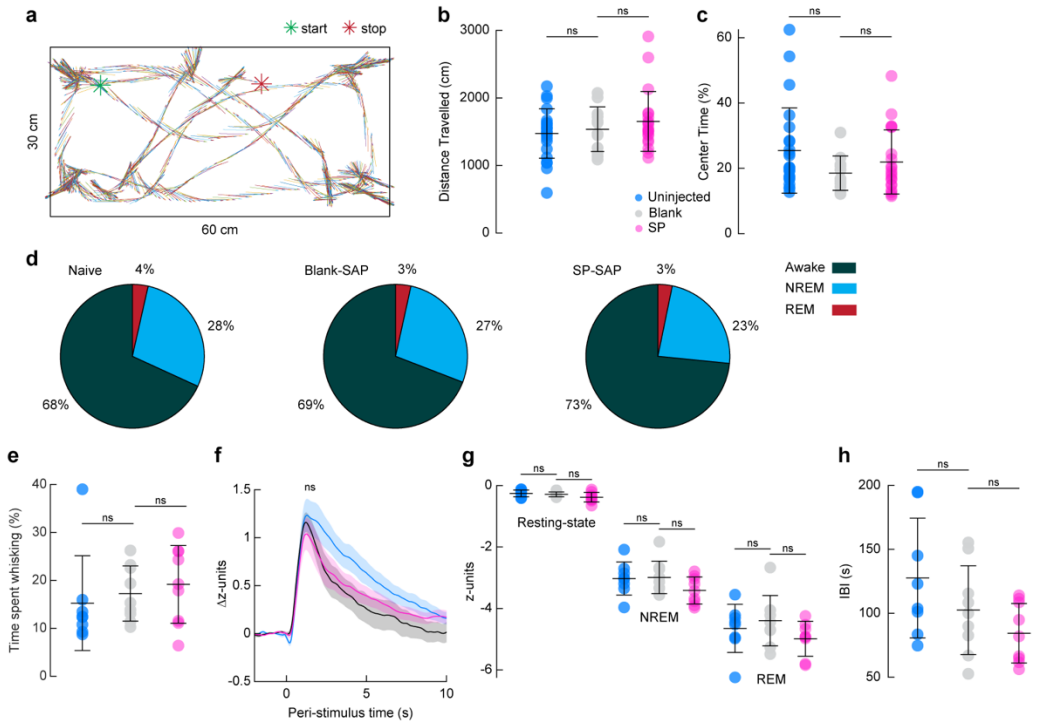

Figure S2. Behavior was unaffected by local ablation of type-I nNOS neurons (a) Example of exploratory behavior during 5 minutes of exploration in a novel environment. **(b)** Total distance traveled during open field exploration. Uninjected mice traveled an average of 1473.4 ± 364.7 cm compared with 1536.6 ± 329.6 cm in Blank-SAP (p = 0.61) and 1652.3 ± 442.7 cm in SP-SAP (p = 0.43). **(c)** Time spent in the center of the open field. Uninjected mice spent on average 25.5 ± 13.1% of total exploration time in the center compared with 18.5 ± 5.3% in Blank-SAP (p = 0.08, GLME) and 21.9 ±9.8% in SP-SAP (p = 0.26). **(b, c)** n = 12-23 mice per group. **(d)** Percentage of time classified in each arousal state by sleep scoring. Uninjected mice spent 68.1 ± 13.2% of the time awake compared to 69.1 ± 15.1% in Blank-SAP (p = 0.89, ttest) and 73.4 ± 11.6% in SP-SAP (p = 0.51, ttest). Uninjected mice spent 28.3 ± 11.1% of the time in NREM sleep compared to 27.4 ± 12.0% in Blank-SAP (p = 0.87, ttest) and 23.4 ± 9.7% in SP-SAP (p = 0.44, ttest). Uninjected mice spent 3.5 ± 2.9% of the time in REM sleep compared to 3.4 ± 3.5% in Blank-SAP (p = 0.96, ttest) and 3.2 ± 2.3% in SP-SAP (p = 0.88, ttest). **(e)** Time spent whisking as a percentage of total imaging time. Uninjected mice spent 15.3 ± 9.9% compared with 17.3 ± 5.8% in Blank-SAP (p = 0.61, ttest) and 19.2 ± 8.1% in SP-SAP (p = 0.75, ttest). **(f)** Change in Pupil diameter in response to vibrissae stimulation. Pupil diameter of uninjected mice increased 1.3 ± 0.5 z-units following vibrissae stimulation compared with 1.2 ± 0.3 z-units in Blank-SAP (p = 0.76, ttest) and 1.1 ± 0.5 z-units in SP-SAP (p = 0.50, ttest). **(g)** Average pupil diameter across arousal states. Average pupil diameter of Uninjected mice during the resting-state was -0.25 ± 0.1 z-units compared with -0.29 ± 0.1 z-units in Blank-SAP (p = 0.45, ttest) and -0.34 ± 0.2 in SP-SAP (p = 0.14, ttest). Average pupil diameter of Uninjected mice during periods of NREM sleep was -3 ± 0.5 z-units compared with -3 ± 0.5 z-units in Blank-SAP (p = 0.89, ttest) and -3.4 ± 0.4 in SP-SAP (p = 0.08, ttest). Average pupil diameter of Uninjected mice during periods of REM sleep was -4.6 ± 0.8 z-units compared with -4.4 ± 0.8 z-units in Blank-SAP (p = 0.53, ttest) and -5 ± 0.6 in SP-SAP (p = 0.11, ttest) **(h)** Interblink-interval. Uninjected mice had a mean interblink-interval of 127.6 ± 46.8 s compared with 102.5 ± 34.7 s in Blank-SAP (p = 0.22, ttest) and 84.5 ± 23.3 s in SP-SAP (p = 0.21, ttest). **(d-h)** n = 9 mice per group. Shading **(f)** indicates SEM and error bars **(b, c, e, g, h)** denote SD. *α < 0.05, **α < 0.01, ***α < 0.001.

580 **Supplemental Figure 3**

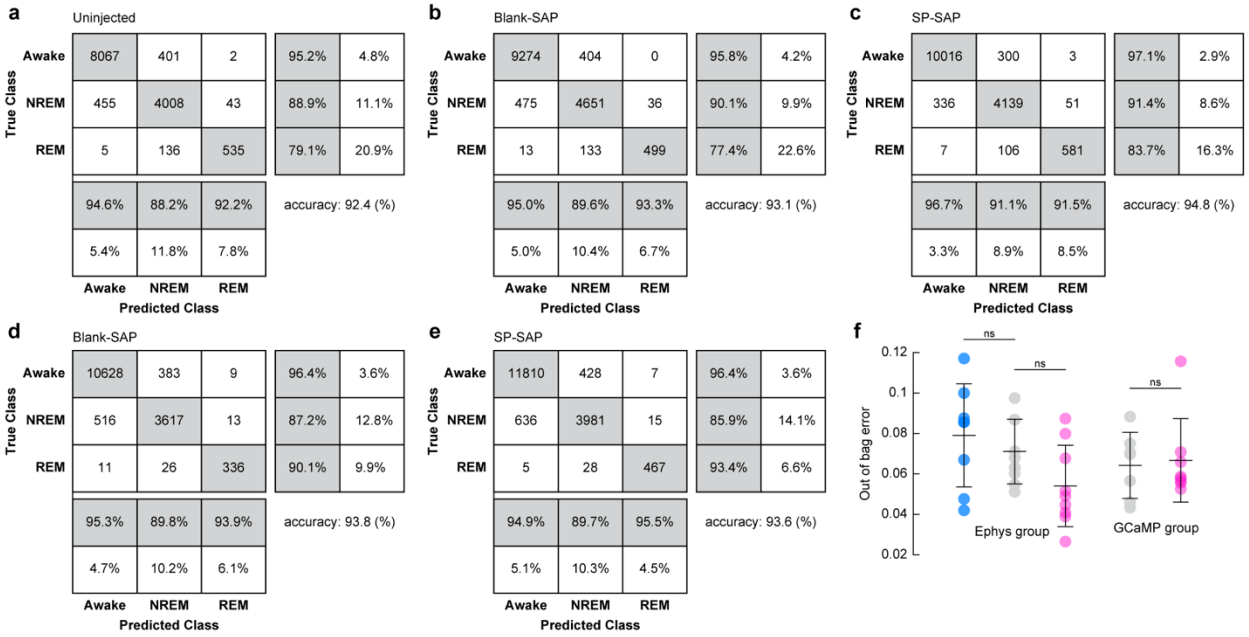

Figure S3. Sleep classification accuracy was unchanged following type-I nNOS ablation (a) Confusion matrix for arousal state classification of Uninjected mice with bilaterally implanted stereotrodes. **(b)** Confusion matrix for arousal state classification of Blank-SAP mice with bilaterally implanted stereotrodes. **(c)** Confusion matrix for arousal state classification of SP-SAP mice with bilaterally implanted stereotrodes. **(a-c)** n = 9 mice per group. **(d)** Confusion matrix for arousal state classification of Blank-SAP mice expressing pan-neuronal GCaMP. **(e)** Confusion matrix for arousal state classification of SP-SAP mice expressing pan-neuronal GCaMP. **(d, e)** n = 6-7 mice per group. **(f)** Out-of-bag error during training of each animal's bootstrapped random forest classification algorithm. For mice with bilateral LFP recordings, Uninjected mice had an average loss of 0.08 ± 0.03 in comparison to 0.07 ± 0.02 in Blank-SAP (p = 0.45, ttest) compared to 0.05 ± 0.02 in SP-SAP (p = 0.064, ttest). Blank-SAP mice with pan-neuronal GCaMP had an average classification loss of 0.06 ± 0.02 compared with 0.07 ± 0.02 in SP-SAP (p = 0.80, ttest). Error bars denote SD. *α < 0.05, **α < 0.01, ***α < 0.001.

581 **Supplemental Figure 4**

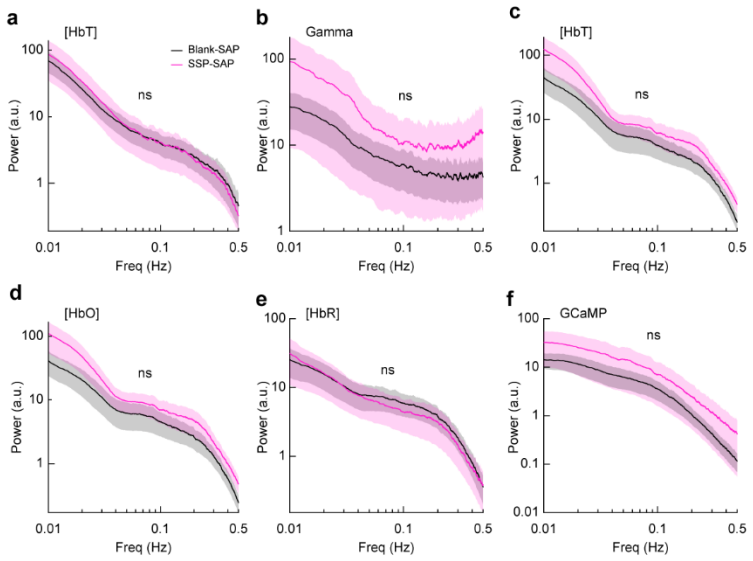

Figure S4. Ablation of Type-I nNOS neurons does not alter hemodynamic or neural power spectra Power spectral density for vascular and hemodynamic signals for the Blank-SAP group (N = 9, 4M/5F for **a, b**; N = 7, 3M/4F for **c-f**) and SP-SAP group (N = 9, 5M/4F for **a, b;** N = 8, 4M/4F for **c-f**) was not significantly different across all measurements of hemodynamic and neural signals. **(a)** Δ[HbT] for electrophysiology animals (p = 0.77, GLME). **(b)** Gamma-band power (second spectra) for animals with electrophysiology (p = 0.19, GLME). **(c)** Δ[HbT] for animals with GCaMP (p = 0.27, GLME). **(d)** Δ[HbT] for animals with GCaMP (p = 0.26, GLME). **(e)** Δ[HbT] for animals with GCaMP (p = 0.68, GLME). **(f)** GCaMP fluorescence (p = 0.44, GLME). Shading represents population averages ± SEM. *α < 0.05, **α < 0.01, ***α < 0.001.

Supplemental Figure 5

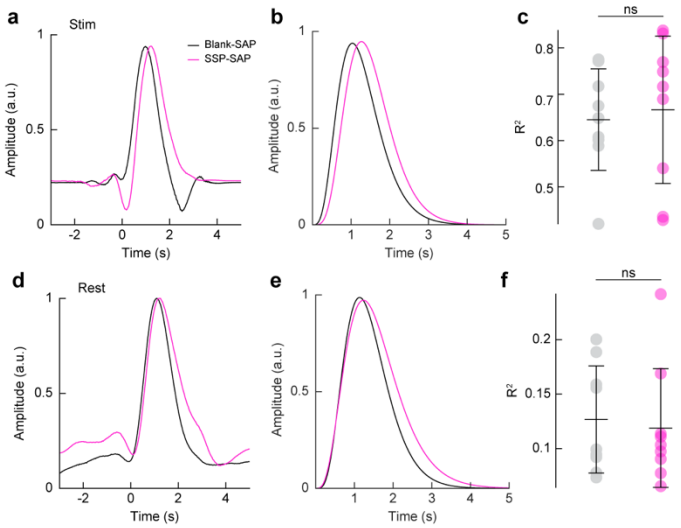

Figure S5. Ablation of Type-I nNOS neurons does not alter the predictive power of the hemodynamic response function (a) Stimulus-evoked hemodynamic response function obtained with deconvolution. **(b)** Stimulus-evoked hemodynamic response function fitted with a gamma distribution function. **(c)** There was no significant difference between the Δ[HbT] predictive R^2 values calculated from impulse-derived HRFs between Blank-SAP (N = 9, 4M/5F) 0.64 ± 0.11 or SP-SAP (N = 9, 5M/4F) 0.67 ± 0.16 following vibrissae stimulation (p = 0.746, ttest). **(d)** Resting-state hemodynamic response function based on deconvolution. **(e)** Resting-state hemodynamic response function fitted with a gamma distribution function. **(f)** There was no significant difference between the Δ[HbT] predictive R^2 values calculated from impulse-derived HRFs between Blank-SAP (N = 9, 4M/5F) 0.13 ± 0.0.05 or SP-SAP (N = 9, 5M/4F) 0.12 ± 0.05 during the resting-state (p = 0.749, ttest). Error bars denote SD. *α < 0.05, **α < 0.01, ***α < 0.001.

583 **Supplemental Figure 6**

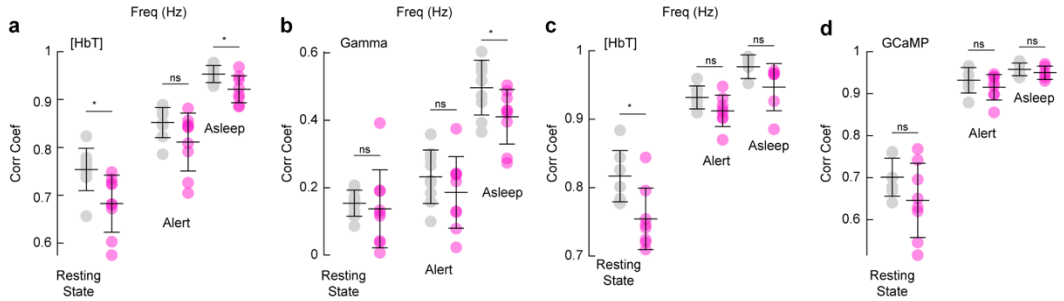

Figure S6. Pearson's correlation coefficients between bilateral hemodynamic and neural signals (a) Correlation coefficient between bilateral hemodynamic signals during the resting-state was 0.75 ± 0.04 in Blank-SAP and 0.68 ± 0.06 in SP-SAP (ttest p = 0.011), during the alert state was 0.85 ± 0.03 with Blank-SAP and 0.81 ± 0.06 in SP-SAP (ttest p = 0.09), and during the asleep state was 0.95 ± 0.02 in Blank-SAP and 0.92 ± 0.03 in SP-SAP (ttest p = 0.01). **(b)** Correlation coefficient between bilateral gamma-band power signals during the resting-state was 0.15 ± 0.04 in Blank-SAP and 0.14 ± 0.12 in SP-SAP (ttest p = 0.69), during the alert state was 0.23 ± 0.08 in Blank-SAP and 0.19 ± 0.11 in SP-SAP (ttest p = 0.31), and during the asleep state was 0.50 ± 0.08 in Blank-SAP and 0.41 ± 0.08 in SP-SAP (ttest p = 0.04). **(c)** Correlation coefficient between bilateral hemodynamic signals (GCaMP7s group) during the resting-state was 0.82 ± 0.04 in Blank-SAP and 0.75 ± 0.04 in SP-SAP (ttest p = 0.01), during the alert state was 0.93 ± 0.02 in Blank-SAP and 0.91 ± 0.02 in SP-SAP (ttest p = 0.08), and during the asleep state was 0.98 ± 0.02 with in-SAP and 0.95 ± 0.03 in SP-SAP (ttest p = 0.07). **(d)** Correlation coefficient between bilateral GCaMP7s signals during the resting-state was 0.70 ± 0.05 in Blank-SAP and 0.65 ± 0.09 in SP-SAP (ttest p = 0.16), during the alert state was 0.93 ± 0.03 with Blank-SAP and 0.92 ± 0.03 in SP-SAP (ttest p = 0.31), and during the asleep state was 0.96 ± 0.02 with Blank-SAP and 0.95 ± 0.02 in SP-SAP (ttest p = 0.37). Error bars denote SD. $\alpha < 0.05$, $^{**}\alpha < 0.01$, $^{***}\alpha < 0.001$.

584 **Supplemental Figure 7**

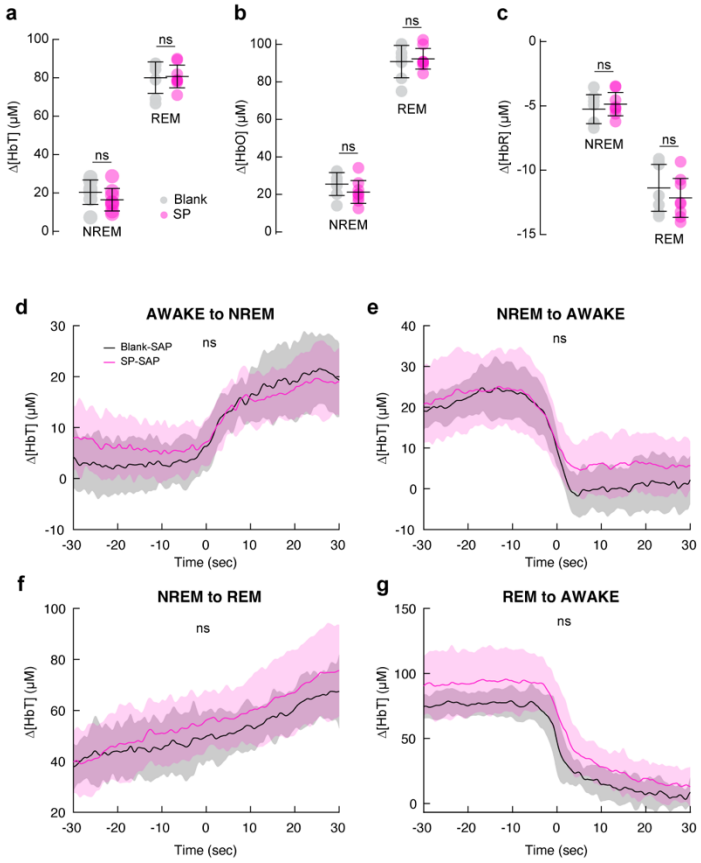

Figure S7. Removal of type-I nNOS neurons did not alter arousal state-related hemodynamic changes (a-c) Average Δ[HbT/O/R] during periods of NREM sleep and REM sleep in mice with pan-neuronal GCaMP (n = 6-7 mice per group). **(a)** NREM Δ[HbT] in Blank-SAP mice was 20.4 ± 6.4 μM compared to 16.5 ± 5.9 μM in SP-SAP (p = 0.27, ttest). REM Δ[HbT] in Blank-SAP mice was 80.0 ± 8.2 μM compared to 80.7 ± 5.9 μM in SP-SAP (p = 0.87, ttest). **(b)** NREM Δ[HbO] in Blank-SAP mice was 25.5 ± 6.1 μM compared to 21.2 ± 6.1 μM in SP-SAP (p = 0.23, ttest). REM Δ[HbO] in Blank-SAP mice was 90.8 ± 8.6 μM compared to 92.3 ± 5.5 μM in SP-SAP (p = 0.72, ttest). **(c)** NREM Δ[HbR] in Blank-SAP mice was -5.3 ± 1.1 μM compared to -4.9 ± 0.9 μM in SP-SAP (p = 0.50, ttest). REM Δ[HbR] in Blank-SAP mice was -11.4 ± 1.8 μM compared to -12.2 ± 1.5 μM in SP-SAP (p = 0.42, ttest). **(d)** Transition from Awake to NREM had a Δ[HbT] of -16.6 ± 6.4 μM in Blank-SAP mice and -11.1 ± 7.0 μM in SP-SAP mice ($p < 0.08$, GLME). **(e)** Transition from NREM to Awake had a Δ[HbT] of 21.5 ± 7.7 μM in Blank-SAP mice and 17.6 ± 9.5 μM in SP-SAP mice ($p < 0.33$, GLME). **(f)** Transition from NREM to REM had a Δ[HbT] of -17.6 ± 3.9 μM in Blank-SAP mice and -22.6 ± 7.9 μM in SP-SAP mice ($p < 0.09$, GLME). **(g)** Transition from REM to Awake had a Δ[HbT] of 67.8 ± 7.3 μM in Blank-SAP mice and 74.0 ± 13.1 μM in SP-SAP mice ($p < 0.21$, GLME). Error bars denote SD. Shading represents population averages ± SEM.*$\alpha < 0.05$, **$\alpha < 0.01$, ***$\alpha < 0.001$.

585 **Supplemental Figure 8**

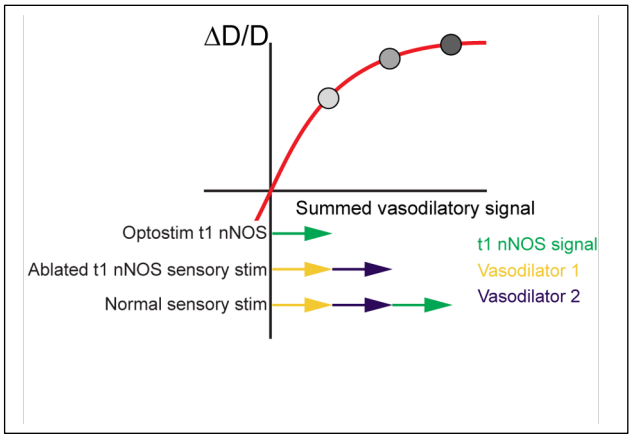

Figure S8. Schematic showing how non-linearity in the dilation response can explain coexistence strong dilation by activation of a pathway, and little change after weakening a pathway. If the diameter is a sublinear function of the sum of vasodilatory inputs, activation of all pathways will cause a dilation that is smaller than the sum of activation of each pathway individually. Loss of one pathway will not cause large changes, even though activation of that pathway in isolation can cause large dilations.

586 **References**

587 Abbott SB, Kanbar R, Bochorishvili G, Coates MB, Stornetta RL, Guyenet PG (2012) C1 neurons excite
588 locus coeruleus and A5 noradrenergic neurons along with sympathetic outflow in rats. J Physiol
589 590:2897-2915. PMC3448155 doi:10.1113/jphysiol.2012.232157

590 Ahn SJ, Anfray A, Anrather J, Iadecola C (2023) Calcium transients in nNOS neurons underlie distinct
591 phases of the neurovascular response to barrel cortex activation in awake mice. J Cereb Blood
592 Flow Metab:271678X231173175. doi:10.1177/0271678X231173175

593 Andrei AR, Debes S, Chelaru M, Liu X, Rodarte E, Spudich JL, Janz R, Dragoi V (2021) Heterogeneous
594 side effects of cortical inactivation in behaving animals. Elife 10. PMC8457825
595 doi:10.7554/eLife.66400

596 Bekar LK, Wei HS, Nedergaard M (2012) The locus coeruleus-norepinephrine network optimizes coupling
597 of cerebral blood volume with oxygen demand. Journal of Cerebral Blood Flow & Metabolism
598 32:2135-2145. doi:10.1038/jcbfm.2012.115

599 Bokil H, Andrews P, Kulkarni JE, Mehta S, Mitra PP (2010) Chronux: a platform for analyzing neural signals.
600 J Neurosci Methods 192:146-151. PMC2934871 doi:10.1016/j.jneumeth.2010.06.020

601 Bredt DS, Glatt CE, Hwang PM, Fotuhi M, Dawson TM, Snyder SH (1991) Nitric oxide synthase protein
602 and mRNA are discretely localized in neuronal populations of the mammalian CNS together with
603 NADPH diaphorase. Neuron 7:615-624. doi:10.1016/0896-6273(91)90374-9

604 Brockway DF, Griffith KR, Aloimonos CM, Clarity TT, Moyer JB, Smith GC, Dao NC, Hossain MS, Drew PJ,
605 Gordon JA, Kupferschmidt DA, Crowley NA (2023) Somatostatin peptide signaling dampens
606 cortical circuits and promotes exploratory behavior. Cell Rep 42:112976. PMC10542913
607 doi:10.1016/j.celrep.2023.112976

608 Bugeon S, Duffield J, Dipoppa M, Ritoux A, Prankerd I, Nicoloutsopoulos D, Orme D, Shinn M, Peng H,
609 Forrest H, Viduolyte A, Reddy CB, Isogai Y, Carandini M, Harris KD (2022) A transcriptomic axis
610 predicts state modulation of cortical interneurons. Nature 607:330-338. PMC9279161
611 doi:10.1038/s41586-022-04915-7

612 Cardin JA, Carlen M, Meletis K, Knoblich U, Zhang F, Deisseroth K, Tsai LH, Moore CI (2009) Driving fast-
613 spiking cells induces gamma rhythm and controls sensory responses. Nature 459:663-667.
614 PMC3655711 doi:10.1038/nature08002

615 Chan KY, Jang MJ, Yoo BB, Greenbaum A, Ravi N, Wu WL, Sanchez-Guardado L, Lois C, Mazmanian
616 SK, Deverman BE, Gradinaru V (2017) Engineered AAVs for efficient noninvasive gene delivery to
617 the central and peripheral nervous systems. Nat Neurosci 20:1172-1179. PMC5529245
618 doi:10.1038/nn.4593

619 Chong PS, Poon CH, Fung ML, Guan L, Steinbusch HWM, Chan YS, Lim WL, Lim LW (2019) Distribution
620 of neuronal nitric oxide synthase immunoreactivity in adult male Sprague-Dawley rat brain. Acta
621 Histochem 121:151437. doi:10.1016/j.acthis.2019.08.004

622 Claron J, Provansal M, Salardaine Q, Tissier P, Dizeux A, Deffieux T, Picaud S, Tanter M, Arcizet F, Pouget
623 P (2023) Co-variations of cerebral blood volume and single neurons discharge during resting state
624 and visual cognitive tasks in non-human primates. Cell Rep 42:112369.
625 doi:10.1016/j.celrep.2023.112369

626 Dana H, Sun Y, Mohar B, Hulse BK, Kerlin AM, Hasseman JP, Tsegaye G, Tsang A, Wong A, Patel R,
627 Macklin JJ, Chen Y, Konnerth A, Jayaraman V, Looger LL, Schreiter ER, Svoboda K, Kim DS
628 (2019) High-performance calcium sensors for imaging activity in neuronal populations and
629 microcompartments. Nat Methods 16:649-657. doi:10.1038/s41592-019-0435-6

630 Dao NC, Suresh Nair M, Magee SN, Moyer JB, Sendao V, Brockway DF, Crowley NA (2020) Forced
631 Abstinence From Alcohol Induces Sex-Specific Depression-Like Behavioral and Neural
632 Adaptations in Somatostatin Neurons in Cortical and Amygdalar Regions. Front Behav Neurosci
633 14:86. PMC7266989 doi:10.3389/fnbeh.2020.00086

634 Dittrich L, Morairty SR, Warrier DR, Kilduff TS (2015) Homeostatic sleep pressure is the primary factor for
635 activation of cortical nNOS/NK1 neurons. Neuropsychopharmacology 40:632-639. PMC4289951
636 doi:10.1038/npp.2014.212

637 Dittrich L, Heiss JE, Warrier DR, Perez XA, Quik M, Kilduff TS (2012) Cortical nNOS neurons co-express
638 the NK1 receptor and are depolarized by Substance P in multiple mammalian species. Front Neural
639 Circuits 6:31. PMC3367498 doi:10.3389/fncir.2012.00031

640 Drew PJ (2019a) Vascular and neural basis of the BOLD signal. Curr Opin Neurobiol 58:61-69.
641 PMC6859204 doi:10.1016/j.conb.2019.06.004

642 Drew PJ, Shih AY, Kleinfeld D (2011) Fluctuating and sensory-induced vasodynamics in rodent cortex
643 extend arteriole capacity. Proc Natl Acad Sci U S A 108:8473-8478. PMC3100929
644 doi:10.1073/pnas.1100428108

645 Drew PJ, Winder AT, Zhang Q (2019b) Twitches, Blinks, and Fidgets: Important Generators of Ongoing
646 Neural Activity. Neuroscientist 25:298-313. PMC6800083 doi:10.1177/1073858418805427

647 Drew PJ, Shih AY, Driscoll JD, Knutsen PM, Blinder P, Davalos D, Akassoglou K, Tsai PS, Kleinfeld D
648 (2010) Chronic optical access through a polished and reinforced thinned skull. Nat Methods 7:981-
649 984. PMC3204312 doi:10.1038/nmeth.1530

650 Echagarruga CT, Gheres KW, Norwood JN, Drew PJ (2020) nNOS-expressing interneurons control basal
651 and behaviorally evoked arterial dilation in somatosensory cortex of mice. Elife 9. PMC7556878
652 doi:10.7554/eLife.60533

653 Endo T, Yanagawa Y, Komatsu Y (2016) Substance P Activates Ca2+-Permeable Nonselective Cation
654 Channels through a Phosphatidylcholine-Specific Phospholipase C Signaling Pathway in nNOS-
655 Expressing GABAergic Neurons in Visual Cortex. Cereb Cortex 26:669-682.
656 doi:10.1093/cercor/bhu233

657 Gao YR, Greene SE, Drew PJ (2015) Mechanical restriction of intracortical vessel dilation by brain tissue
658 sculpts the hemodynamic response. Neuroimage 115:162-176. PMC4470397
659 doi:10.1016/j.neuroimage.2015.04.054

660 Gerashchenko D, Schmidt MA, Zielinski MR, Moore ME, Wisor JP (2018) Sleep State Dependence of
661 Optogenetically evoked Responses in Neuronal Nitric Oxide Synthase-positive Cells of the
662 Cerebral Cortex. Neuroscience 379:189-201. PMC6311348
663 doi:10.1016/j.neuroscience.2018.02.006

664 Gerashchenko D, Wisor JP, Burns D, Reh RK, Shiromani PJ, Sakurai T, de la Iglesia HO, Kilduff TS (2008)
665 Identification of a population of sleep-active cerebral cortex neurons. Proc Natl Acad Sci U S A
666 105:10227-10232. PMC2481371 doi:10.1073/pnas.0803125105

667 Gheres KW, Unsal HS, Han X, Zhang Q, Turner KL, Zhang N, Drew PJ (2023) Arousal state transitions
668 occlude sensory-evoked neurovascular coupling in neonatal mice. Commun Biol 6:738.
669 PMC10352318 doi:10.1038/s42003-023-05121-5

670 Hablitz LM, Vinitsky HS, Sun Q, Staeger FF, Sigurdsson B, Mortensen KN, Lilius TO, Nedergaard M (2019)
671 Increased glymphatic influx is correlated with high EEG delta power and low heart rate in mice
672 under anesthesia. Sci Adv 5:eaav5447. PMC6392807 doi:10.1126/sciadv.aav5447

673 Han K, Min J, Lee M, Kang BM, Park T, Hahn J, Yei J, Lee J, Woo J, Lee CJ, Kim SG, Suh M (2019)
674 Neurovascular Coupling under Chronic Stress Is Modified by Altered GABAergic Interneuron
675 Activity. J Neurosci 39:10081-10095. PMC6978951 doi:10.1523/JNEUROSCI.1357-19.2019

676 Haselden WD, Kedarasetti RT, Drew PJ (2020) Spatial and temporal patterns of nitric oxide diffusion and
677 degradation drive emergent cerebrovascular dynamics. PLoS Comput Biol 16:e1008069.
678 PMC7410342 doi:10.1371/journal.pcbi.1008069

679 He M, Tucciarone J, Lee S, Nigro MJ, Kim Y, Levine JM, Kelly SM, Krugikov I, Wu P, Chen Y, Gong L, Hou
680 Y, Osten P, Rudy B, Huang ZJ (2016) Strategies and Tools for Combinatorial Targeting of
681 GABAergic Neurons in Mouse Cerebral Cortex. Neuron 91:1228-1243. PMC5223593
682 doi:10.1016/j.neuron.2016.08.021

683 Hendry SH, Schwark HD, Jones EG, Yan J (1987) Numbers and proportions of GABA-immunoreactive
684 neurons in different areas of monkey cerebral cortex. J Neurosci 7:1503-1519. PMC6568832
685 doi:10.1523/JNEUROSCI.07-05-01503.1987

686 Higo S, Udaka N, Tamamaki N (2007) Long-range GABAergic projection neurons in the cat neocortex. J
687 Comp Neurol 503:421-431. doi:10.1002/cne.21395

688 Hill CE (2012) Long Distance Conduction of Vasodilation: A Passive or Regenerative Process?
689 Microcirculation 19:379-390. doi:10.1111/j.1549-8719.2012.00169.x

690 Holstein-Ronsbo S, Gan Y, Giannetto MJ, Rasmussen MK, Sigurdsson B, Beinlich FRM, Rose L, Untiet V,
691 Hablitz LM, Kelley DH, Nedergaard M (2023) Glymphatic influx and clearance are accelerated by
692 neurovascular coupling. Nat Neurosci. doi:10.1038/s41593-023-01327-2

693 Hope BT, Vincent SR (1989) Histochemical characterization of neuronal NADPH-diaphorase. J Histochem
694 Cytochem 37:653-661. doi:10.1177/37.5.2703701

695 Hope BT, Michael GJ, Knigge KM, Vincent SR (1991) Neuronal NADPH diaphorase is a nitric oxide
696 synthase. Proc Natl Acad Sci U S A 88:2811-2814. PMC51329 doi:10.1073/pnas.88.7.2811

697 Hosford PS, Gourine AV (2019) What is the key mediator of the neurovascular coupling response? Neurosci
698 Biobehav Rev 96:174-181. PMC6331662 doi:10.1016/j.neubiorev.2018.11.011

699 Huang H, Kuzirian MS, Cai X, Snyder LM, Cohen J, Kaplan DH, Ross SE (2016) Generation of a NK1R-
700 CreER knockin mouse strain to study cells involved in Neurokinin 1 Receptor signaling. Genesis
701 54:593-601. PMC5241089 doi:10.1002/dvg.22985

702 Huo BX, Smith JB, Drew PJ (2014) Neurovascular coupling and decoupling in the cortex during voluntary
703 locomotion. J Neurosci 34:10975-10981. PMC4131012 doi:10.1523/JNEUROSCI.1369-14.2014

704 Huo BX, Gao YR, Drew PJ (2015) Quantitative separation of arterial and venous cerebral blood volume
705 increases during voluntary locomotion. Neuroimage 105:369-379. PMC4330110
706 doi:10.1016/j.neuroimage.2014.10.030

707 Iadecola C, Smith EE, Anrather J, Gu C, Mishra A, Misra S, Perez-Pinzon MA, Shih AY, Sorond FA, van
708 Veluw SJ, Wellington CL, American Heart Association Stroke C, Council on Arteriosclerosis T,
709 Vascular B, Council on Cardiovascular R, Intervention, Council on H, Council on L, Cardiometabolic
710 H (2023) The Neurovasculome: Key Roles in Brain Health and Cognitive Impairment: A Scientific
711 Statement From the American Heart Association/American Stroke Association. Stroke.
712 doi:10.1161/STR.0000000000000431

713 Jiang-Xie LF, Drieu A, Bhasiin K, Quintero D, Smirnov I, Kipnis J (2024) Neuronal dynamics direct
714 cerebrospinal fluid perfusion and brain clearance. Nature 627:157-164. doi:10.1038/s41586-024-
715 07108-6

716 Kara P, Friedlander MJ (1999) Arginine analogs modify signal detection by neurons in the visual cortex. J
717 Neurosci 19:5528-5548. PMC6782344 doi:10.1523/JNEUROSCI.19-13-05528.1999

718 Karagiannis A, Gallopin T, David C, Battaglia D, Geoffroy H, Rossier J, Hillman EM, Staiger JF, Cauli B
719 (2009) Classification of NPY-expressing neocortical interneurons. J Neurosci 29:3642-3659.
720 PMC2750888 doi:10.1523/JNEUROSCI.0058-09.2009

721 Kawaguchi Y, Kubota Y (1997) GABAergic cell subtypes and their synaptic connections in rat frontal cortex.
722 Cereb Cortex 7:476-486. doi:10.1093/cercor/7.6.476

723 Kedarasetti RT, Drew PJ, Costanzo F (2022) Arterial vasodilation drives convective fluid flow in the brain:
724 a poroelastic model. Fluids Barriers CNS 19:34. PMC9107702 doi:10.1186/s12987-022-00326-y

725 Kilduff TS, Cauli B, Gerashchenko D (2011) Activation of cortical interneurons during sleep: an anatomical
726 link to homeostatic sleep regulation? Trends Neurosci 34:10-19. PMC3014438
727 doi:10.1016/j.tins.2010.09.005

728 Kjaerby C, Andersen M, Hauglund N, Untiet V, Dall C, Sigurdsson B, Ding F, Feng J, Li Y, Weikop P, Hirase
729 H, Nedergaard M (2022) Memory-enhancing properties of sleep depend on the oscillatory
730 amplitude of norepinephrine. Nat Neurosci 25:1059-1070. PMC9817483 doi:10.1038/s41593-022-
731 01102-9

732 Knot HJ, Nelson MT (1998) Regulation of arterial diameter and wall [Ca2+] in cerebral arteries of rat by
733 membrane potential and intravascular pressure. The Journal of Physiology 508 (Pt 1:199-209.

Kramer RS, Pearlstein RD (1979) Cerebral cortical microfluorometry at isosbestic wavelengths for correction of vascular artifact. Science 205:693-696. doi:10.1126/science.223243

Krawchuk MB, Ruff CF, Yang X, Ross SE, Vazquez AL (2020) Optogenetic assessment of VIP, PV, SOM and NOS inhibitory neuron activity and cerebral blood flow regulation in mouse somato-sensory cortex. J Cereb Blood Flow Metab 40:1427-1440. PMC7307010 doi:10.1177/0271678X19870105

Kress BT, Iliff JJ, Xia M, Wang M, Wei HS, Zeppenfeld D, Xie L, Kang H, Xu Q, Liew JA, Plog BA, Ding F, Deane R, Nedergaard M (2014) Impairment of paravascular clearance pathways in the aging brain. Annals of Neurology 76:845-861. doi:10.1002/ana.24271

Kubota Y, Shigematsu N, Karube F, Sekigawa A, Kato S, Yamaguchi N, Hirai Y, Morishima M, Kawaguchi Y (2011) Selective coexpression of multiple chemical markers defines discrete populations of neocortical GABAergic neurons. Cereb Cortex 21:1803-1817. doi:10.1093/cercor/bhq252

Lee L, Boorman L, Glendenning E, Christmas C, Sharp P, Redgrave P, Shabir O, Bracci E, Berwick J, Howarth C (2020) Key Aspects of Neurovascular Control Mediated by Specific Populations of Inhibitory Cortical Interneurons. Cereb Cortex 30:2452-2464. PMC7174996 doi:10.1093/cercor/bhz251

Li N, Chen S, Guo ZV, Chen H, Huo Y, Inagaki HK, Chen G, Davis C, Hansel D, Guo C, Svoboda K (2019) Spatiotemporal constraints on optogenetic inactivation in cortical circuits. Elife 8. PMC6892606 doi:10.7554/eLife.48622

Ma Y, Shaik MA, Kozberg MG, Kim SH, Portes JP, Timerman D, Hillman EM (2016a) Resting-state hemodynamics are spatiotemporally coupled to synchronized and symmetric neural activity in excitatory neurons. Proc Natl Acad Sci U S A 113:E8463-E8471. PMC5206542 doi:10.1073/pnas.1525369113

Ma Y, Shaik MA, Kim SH, Kozberg MG, Thibodeaux DN, Zhao HT, Yu H, Hillman EM (2016b) Wide-field optical mapping of neural activity and brain haemodynamics: considerations and novel approaches. Philos Trans R Soc Lond B Biol Sci 371. PMC5003860 doi:10.1098/rstb.2015.0360

Martin JL, Sloviter RS (2001) Focal inhibitory interneuron loss and principal cell hyperexcitability in the rat hippocampus after microinjection of a neurotoxic conjugate of saporin and a peptidase-resistant analog of Substance P. The Journal of Comparative Neurology 436:127-152. doi:10.1002/cne.1065

Mathis A, Mamidanna P, Cury KM, Abe T, Murthy VN, Mathis MW, Bethge M (2018) DeepLabCut: markerless pose estimation of user-defined body parts with deep learning. Nat Neurosci 21:1281-1289. doi:10.1038/s41593-018-0209-y

Matrongolo MJ, Ang PS, Wu J, Jain A, Thackray JK, Reddy A, Sung CC, Barbet G, Hong Y-K, Tischfield MA (2023) Piezo1 agonist restores meningeal lymphatic vessels, drainage, and brain-CSF perfusion in craniosynostosis and aged mice. Journal of Clinical Investigation 134. doi:10.1172/jci171468

Matsumura S, Yamamoto K, Nakaya Y, O'Hashi K, Kaneko K, Takei H, Tsuda H, Shirakawa T, Kobayashi M (2021) Presynaptic NK1 Receptor Activation by Substance P Suppresses EPSCs via Nitric Oxide

Synthesis in the Rat Insular Cortex. Neuroscience 455:151-164. doi:10.1016/j.neuroscience.2020.12.012

McKay LC, Feldman JL (2008) Unilateral ablation of pre-Botzinger complex disrupts breathing during sleep but not wakefulness. Am J Respir Crit Care Med 178:89-95. PMC2441928 doi:10.1164/rccm.200712-1901OC

Morairty SR, Dittrich L, Pasumarthi RK, Valladao D, Heiss JE, Gerashchenko D, Kilduff TS (2013) A role for cortical nNOS/NK1 neurons in coupling homeostatic sleep drive to EEG slow wave activity. Proc Natl Acad Sci U S A 110:20272-20277. PMC3864296 doi:10.1073/pnas.1314762110

Osorio-Forero A, Cardis R, Vantomme G, Guillaume-Gentil A, Katsioudi G, Devenoges C, Fernandez LMJ, Luthi A (2021) Noradrenergic circuit control of non-REM sleep substates. Curr Biol 31:5009-5023 e5007. doi:10.1016/j.cub.2021.09.041

Paul A, Crow M, Raudales R, He M, Gillis J, Huang ZJ (2017) Transcriptional Architecture of Synaptic Communication Delineates GABAergic Neuron Identity. Cell 171:522-539 e520. PMC5772785 doi:10.1016/j.cell.2017.08.032

Penny GR, Afsharpour S, Kitai ST (1986) Substance P-immunoreactive neurons in the neocortex of the rat: A subset of the glutamic acid decarboxylase-immunoreactive neurons. Neuroscience Letters 65:53-59. doi:10.1016/0304-3940(86)90119-9

Perrenoud Q, Geoffroy H, Gauthier B, Rancillac A, Alfonsi F, Kessaris N, Rossier J, Vitalis T, Gallopin T (2012) Characterization of Type I and Type II nNOS-Expressing Interneurons in the Barrel Cortex of Mouse. Front Neural Circuits 6:36. PMC3386492 doi:10.3389/fncir.2012.00036

Pfeffer CK, Xue M, He M, Huang ZJ, Scanziani M (2013) Inhibition of inhibition in visual cortex: the logic of connections between molecularly distinct interneurons. Nat Neurosci 16:1068-1076. PMC3729586 doi:10.1038/nn.3446

Phillips EA, Hasenstaub AR (2016) Asymmetric effects of activating and inactivating cortical interneurons. Elife 5. PMC5123863 doi:10.7554/eLife.18383

Pleil KE, Rinker JA, Lowery-Gionta EG, Mazzone CM, McCall NM, Kendra AM, Olson DP, Lowell BB, Grant KA, Thiele TE, Kash TL (2015) NPY signaling inhibits extended amygdala CRF neurons to suppress binge alcohol drinking. Nat Neurosci 18:545-552. PMC4376619 doi:10.1038/nn.3972

Roth KA, Katz RJ (1979) Stress, behavioral arousal, and open field activity--a reexamination of emotionality in the rat. Neurosci Biobehav Rev 3:247-263. doi:10.1016/0149-7634(79)90012-5

Ruff CF, Juarez Anaya F, Dienel SJ, Rakymzhan A, Altamirano-Espinoza A, Couey JJ, Fukuda M, Watson AM, Su A, Fish KN, Rubio ME, Hooks BM, Ross SE, Vazquez AL (2024) Long-range inhibitory neurons mediate cortical neurovascular coupling. Cell Rep 43:113970. doi:10.1016/j.celrep.2024.113970

Sahara S, Yanagawa Y, O'Leary DD, Stevens CF (2012) The fraction of cortical GABAergic neurons is constant from near the start of cortical neurogenesis to adulthood. J Neurosci 32:4755-4761. PMC3325497 doi:10.1523/JNEUROSCI.6412-11.2012

809 Schaeffer S, Iadecola C (2021) Revisiting the neurovascular unit. Nat Neurosci 24:1198-1209.
810 doi:10.1038/s41593-021-00904-7

811 Scherer-Singler U, Vincent SR, Kimura H, McGeer EG (1983) Demonstration of a unique population of
812 neurons with NADPH-diaphorase histochemistry. J Neurosci Methods 9:229-234.
813 doi:10.1016/0165-0270(83)90085-7

814 Scott BB, Thiberge SY, Guo C, Tervo DGR, Brody CD, Karpova AY, Tank DW (2018) Imaging Cortical
815 Dynamics in GCaMP Transgenic Rats with a Head-Mounted Widefield Macroscope. Neuron
816 100:1045-1058 e1045. PMC6283673 doi:10.1016/j.neuron.2018.09.050

817 Seibenhener ML, Wooten MC (2015) Use of the Open Field Maze to measure locomotor and anxiety-like
818 behavior in mice. J Vis Exp:e52434. PMC4354627 doi:10.3791/52434

819 Shih AY, Mateo C, Drew PJ, Tsai PS, Kleinfeld D (2012) A Polished and Reinforced Thinned-skull Window
820 for Long-term Imaging of the Mouse Brain. Journal of Visualized Experiments. doi:10.3791/3742-
821 v

822 Sicher AR, Starnes WD, Griffith KR, Dao NC, Smith GC, Brockway DF, Crowley NA (2023) Adolescent
823 binge drinking leads to long-lasting changes in cortical microcircuits in mice. Neuropharmacology
824 234:109561. PMC10386078 doi:10.1016/j.neuropharm.2023.109561

825 Sirotin YB, Das A (2009) Anticipatory haemodynamic signals in sensory cortex not predicted by local
826 neuronal activity. Nature 457:475-479. PMC2705195 doi:10.1038/nature07664

827 Smith RJ, Anderson RI, Haun HL, Mulholland PJ, Griffin WC, 3rd, Lopez MF, Becker HC (2020) Dynamic
828 c-Fos changes in mouse brain during acute and protracted withdrawal from chronic intermittent
829 ethanol exposure and relapse drinking. Addict Biol 25:e12804. PMC7579841
830 doi:10.1111/adb.12804

831 Smith SL, Otis TS (2003) Persistent changes in spontaneous firing of Purkinje neurons triggered by the
832 nitric oxide signaling cascade. J Neurosci 23:367-372.

833 Sohal VS, Zhang F, Yizhar O, Deisseroth K (2009) Parvalbumin neurons and gamma rhythms enhance
834 cortical circuit performance. Nature 459:698-702. PMC3969859 doi:10.1038/nature07991

835 Staiger JF, Petersen CCH (2021) Neuronal Circuits in Barrel Cortex for Whisker Sensory Perception.
836 Physiol Rev 101:353-415. doi:10.1152/physrev.00019.2019

837 Stringer C, Pachitariu M, Steinmetz N, Reddy CB, Carandini M, Harris KD (2019) Spontaneous behaviors
838 drive multidimensional, brainwide activity. Science 364:255. PMC6525101
839 doi:10.1126/science.aav7893

840 Tomioka R, Rockland KS (2007) Long-distance corticocortical GABAergic neurons in the adult monkey
841 white and gray matter. J Comp Neurol 505:526-538. doi:10.1002/cne.21504

842 Tomioka R, Okamoto K, Furuta T, Fujiyama F, Iwasato T, Yanagawa Y, Obata K, Kaneko T, Tamamaki N
843 (2005) Demonstration of long-range GABAergic connections distributed throughout the mouse
844 neocortex. Eur J Neurosci 21:1587-1600. doi:10.1111/j.1460-9568.2005.03989.x

845 Tricoire L, Vitalis T (2012) Neuronal nitric oxide synthase expressing neurons: a journey from birth to
846 neuronal circuits. Front Neural Circuits 6:82. PMC3514612 doi:10.3389/fncir.2012.00082

847 Tu W, Cramer SR, Zhang N (2024) Disparity in temporal and spatial relationships between resting-state
848 electrophysiological and fMRI signals. Elife 13. PMC11299978 doi:10.7554/eLife.95680

849 Turner KL, Gheres KW, Drew PJ (2023) Relating Pupil Diameter and Blinking to Cortical Activity and
850 Hemodynamics across Arousal States. J Neurosci 43:949-964. PMC9908322
851 doi:10.1523/JNEUROSCI.1244-22.2022

852 Turner KL, Gheres KW, Proctor EA, Drew PJ (2020) Neurovascular coupling and bilateral connectivity
853 during NREM and REM sleep. Elife 9. PMC7758068 doi:10.7554/eLife.62071

854 Turrigiano GG (2008) The self-tuning neuron: synaptic scaling of excitatory synapses. Cell 135:422-435.
855 PMC2834419 doi:10.1016/j.cell.2008.10.008

856 Uhlirova H et al. (2016) Cell type specificity of neurovascular coupling in cerebral cortex. Elife 5.
857 PMC4933561 doi:10.7554/eLife.14315

858 van Veluw SJ, Hou SS, Calvo-Rodriguez M, Arbel-Ornath M, Snyder AC, Frosch MP, Greenberg SM,
859 Bacskai BJ (2020) Vasomotion as a Driving Force for Paravascular Clearance in the Awake Mouse
860 Brain. Neuron 105:549-561 e545. PMC7028316 doi:10.1016/j.neuron.2019.10.033

861 Vanlandewijck M, He L, Mae MA, Andrae J, Ando K, Del Gaudio F, Nahar K, Lebouvier T, Lavina B, Gouveia
862 L, Sun Y, Raschperger E, Rasanen M, Zarb Y, Mochizuki N, Keller A, Lendahl U, Betsholtz C (2018)
863 A molecular atlas of cell types and zonation in the brain vasculature. Nature 554:475-480.
864 doi:10.1038/nature25739

865 Vo TT, Im GH, Han K, Suh M, Drew PJ, Kim SG (2023) Parvalbumin interneuron activity drives fast
866 inhibition-induced vasoconstriction followed by slow substance P-mediated vasodilation. Proc Natl
867 Acad Sci U S A 120:e2220777120. PMC10161000 doi:10.1073/pnas.2220777120

868 Vruwink M, Schmidt HH, Weinberg RJ, Burette A (2001) Substance P and nitric oxide signaling in cerebral
869 cortex: anatomical evidence for reciprocal signaling between two classes of interneurons. J Comp
870 Neurol 441:288-301. doi:10.1002/cne.1413

871 Wang H, Germanson TP, Guyenet PG (2002) Depressor and tachypneic responses to chemical stimulation
872 of the ventral respiratory group are reduced by ablation of neurokinin-1 receptor-expressing
873 neurons. J Neurosci 22:3755-3764. PMC6758381 doi:10.1523/JNEUROSCI.22-09-03755.2002

874 Wiley RG, Lappi DA (1999) Targeting neurokinin-1 receptor-expressing neurons with [Sar9,Met(O2)11
875 substance P-saporin. Neurosci Lett 277:1-4. doi:10.1016/s0304-3940(99)00846-0

876 Winder AT, Echagarruga C, Zhang Q, Drew PJ (2017) Weak correlations between hemodynamic signals
877 and ongoing neural activity during the resting state. Nat Neurosci 20:1761-1769. PMC5816345
878 doi:10.1038/s41593-017-0007-y

Wölfle SE, Chaston DJ, Goto K, Sandow SL, Edwards FR, Hill CE (2011) Non-linear relationship between hyperpolarisation and relaxation enables long distance propagation of vasodilatation. The Journal of physiology 589:2607-2623. doi:10.1113/jphysiol.2010.202580

Wright PW, Brier LM, Bauer AQ, Baxter GA, Kraft AW, Reisman MD, Bice AR, Snyder AZ, Lee JM, Culver JP (2017) Functional connectivity structure of cortical calcium dynamics in anesthetized and awake mice. PLoS One 12:e0185759. PMC5648115 doi:10.1371/journal.pone.0185759

Wu YT, Bennett HC, Chon U, Vanselow DJ, Zhang Q, Munoz-Castaneda R, Cheng KC, Osten P, Drew PJ, Kim Y (2022) Quantitative relationship between cerebrovascular network and neuronal cell types in mice. Cell Rep 39:110978. PMC9271215 doi:10.1016/j.celrep.2022.110978

Yan XX, Garey LJ (1997) Morphological diversity of nitric oxide synthesising neurons in mammalian cerebral cortex. J Hirnforsch 38:165-172.

Yan XX, Jen LS, Garey LJ (1996) NADPH-diaphorase-positive neurons in primate cerebral cortex colocalize with GABA and calcium-binding proteins. Cereb Cortex 6:524-529. doi:10.1093/cercor/6.3.524

Zhang Q, Haselden WD, Charpak S, Drew PJ (2023) Could respiration-driven blood oxygen changes modulate neural activity? Pflugers Arch 475:37-48. PMC9794637 doi:10.1007/s00424-022-02721-8

Zhang Q, Turner KL, Gheres KW, Hossain MS, Drew PJ (2022) Behavioral and physiological monitoring for awake neurovascular coupling experiments: a how-to guide. Neurophotonics 9:021905. PMC8802326 doi:10.1117/1.NPh.9.2.021905

Zhang Q, Roche M, Gheres KW, Chaigneau E, Kedarasetti RT, Haselden WD, Charpak S, Drew PJ (2019) Cerebral oxygenation during locomotion is modulated by respiration. Nat Commun 10:5515. PMC6893036 doi:10.1038/s41467-019-13523-5

Zhao J, Manza P, Wiers C, Song H, Zhuang P, Gu J, Shi Y, Wang G-J, He D (2020) Age-Related Decreases in Interhemispheric Resting-State Functional Connectivity and Their Relationship With Executive Function. Frontiers in Aging Neuroscience 12. doi:10.3389/fnagi.2020.00020

Zielinski MR, Atochin DN, McNally JM, McKenna JT, Huang PL, Strecker RE, Gerashchenko D (2019) Somatostatin+/nNOS+ neurons are involved in delta electroencephalogram activity and cortical-dependent recognition memory. Sleep 42. PMC6783898 doi:10.1093/sleep/zsz143